Eigenchannel Analysis of Super-Resolution Far-Field Sensing with a Randomly Scattering Analyzer

Justin A. Patel, Qiaoen Luo, and Kevin J. Webb*
Purdue University, West Lafayette, Indiana 47907-2035, USA
(Dated: January 23, 2023)

A method of analysis for a randomly scattering analyzer offering far-subwavelength spatial resolution with coherent light is presented, and the attributes are supported by numerical simulations. Without constraints, far-field detection generally results in a spatial resolution of about one wavelength, mathematically explained through the loss of the evanescent field information in a plane wave expansion. Enhanced spatial resolution is shown to be possible because of relative motion with a structured field and the resulting information available. It is shown that detected information through a scattering analyzer results in enhanced spatial sensitivity with motion of an object in a structured field, and that this is accompanied by changes in the relative distribution of significant eigenvalues of the transmission matrix modeling the analyzer. Thus, the character of the random analyzer is shown to influence the far-field spatial resolution. A random analyzer in principle allows subwavelength sensitivity whose resolution is limited only by measurement accuracy and precision, when fields are scattered from a moving object, or when some other relative change causes a modified field. Consequently, use of a random analyzer offers substantial impact in a variety of applications.

I. INTRODUCTION

The physics of disordered media is of substantial importance in quantum transport and statistical optics, with broad ramifications that include the modeling of small-scale electronic devices and imaging through scattering media. Fundamentally, despite the information that in principle exists in heavily scattered coherent waves, extraction or control remains challenging. We describe the concept of super-resolution spatial sensitivity from changes in the position (motion) of an object with a structured coherent background field, when measurements are made through a randomly scattering analyzer slab. Despite being in the far field, subwavelength spatial information about a moving object becomes available, and the sensitivity relates to the properties of the random analyzer. Experiments indicate far-subwavelength motion sensitivity [1], and these results are investigated in relation to extracting subwavelength (super-resolution) spatial information about an object using numerical simulations in conjunction with a presented method of analysis that involves the eigenvalue decomposition of random matrices. Breaking the (far-field, wavelength-scale) diffraction limit on spatial resolution, without resorting to fluorescence and use of the point spread function of a microscope, opens new scientific and application domains.

The substantial theoretical contributions related to electronic transport in disordered wires (see, for example, [2]) have been drawn upon by work to model the propagation of electromagnetic waves through scattering media via the transmission matrix [3, 4]. Understanding how to determine the eigenchannels in random media is a critical step to the coupling of coherent optical waves into these channels [5, 6]. With control of these input channels, such as by using a spatial light modulator, it becomes possible to focus laser light through substantial amounts of scatter, as would occur in biological tissue. While random scatter of light is limiting in some situations, it has been exploited in the concept of a random spectrometer, where the frequency-dependent transmission of a multimode optical fiber provides sensitivity in measured speckle to changes in frequency [7]. We provide a new dimension to randomly scattering material acting as an analyzer for enhanced sensing of geometrical features from spatial changes in the incident field. These changes could be due to motion of a scatterer or set of scatterers, or the result of small deformations in a solid state material.

This paper explores the topic of randomly scattering analyzers using random matrix theory. It is shown that the ability of such an analyzer to enhance sensitivity is accompanied by certain changes in the probability distribution of the eigenvalues of the transmission matrix that models the analyzer. This builds on the concept of object motion in structured illumination [8, 9]. A randomly scattering analyzer is used to greatly enhance far-field sensitivity to a subwavelength change, with insight into how such enhancement may be improved upon.

In this work, motion is modeled quasi-statically, so that the object in question can be considered stationary at each discrete time step while the fields in question are measured or calculated. Also, because our analysis focuses primarily on sensing and not imaging, we use the term "resolution" to refer to the length scale of the object's geometrical differences that can be distinguished by a sensing system, without assuming that an image can be formed with detail at this length scale (but with the implication that information to do so is in principle available).

Section II begins with a mathematical description that links speckle intensity correlations through a scattering

* Corresponding author: webb@purdue.edu

analyzer to the eigenvalue distribution of the analyzer's transmission matrix. Section III then describes the FEM (finite element method) simulations that demonstrate the relationship between the amount of scatter in the analyzer and the eigenvalue distribution, and these results are examined in Sect. IV by comparing them to existing distributions from the literature. These comparisons show only partial agreement with the bimodal distribution, with improvement demonstrated when the amount of scatter is increased, yet good agreement with the quarter-circle distribution, despite only partial fulfillment of the distribution's requirements. An illustrative example is given in Sect. V, demonstrating that the presence of a scattering analyzer greatly improves far-field sensitivity to a subwavelength feature change. Discussion and conclusion sections follow.

II. CORRELATIONS AND EIGENVALUES

In this section, we formulate intensity correlations representative of measured data in terms of field correlations. This allows us to incorporate the field transmission matrix associated with the randomly scattering analyzer, which we investigate using random matrix theory in Sect. IV.

For this derivation, we assume zero-mean circular Gaussian statistics for the detected field [10], which have been found in previous experiments and numerical simulations [1] involving a scattering analyzer. This derivation and the following eigenvalue simulations in Sect. III therefore collectively provide a deeper understanding of the underlying mechanisms that result in enhanced sensitivity. However, as will be demonstrated in Sect. V, such statistics are merely sufficient, but not necessary, for achieving subwavelength far-field sensitivity.

Assuming Gaussian statistics allows us to apply what is sometimes known as the "complex Gaussian moment theorem" [10, 11] and write the ensemble-averaged intensity correlation in terms of the correlation of the detected fields (through a polarizer) $\Phi(\mathbf{r}_d)$ at different object positions $\mathbf{r}$ and $\mathbf{r}+\Delta\mathbf{r}$ as

$$\langle \tilde{I}(\mathbf{r}_d;\mathbf{r})\tilde{I}(\mathbf{r}_d;\mathbf{r}+\Delta\mathbf{r})\rangle = \frac{|\langle \Phi^*(\mathbf{r}_d;\mathbf{r})\Phi(\mathbf{r}_d;\mathbf{r}+\Delta\mathbf{r})\rangle|^2}{\langle I(\mathbf{r}_d;\mathbf{r})\rangle\langle I(\mathbf{r}_d;\mathbf{r}+\Delta\mathbf{r})\rangle}, \tag{1}$$

where * represents complex conjugation, $\mathbf{r}_d$ is the detector position, which is fixed, and the intensities are normalized as $\tilde{I} = (I - \langle I\rangle)/\langle I\rangle$. The $\langle\cdot\rangle$ is mathematically a configurational average over the random scatterer locations (but obtained experimentally from speckle intensity data captured by a camera [8]). Equation (1) is relevant to the extraction of information about moving objects inside scattering media with coherent fields [12].

However, we seek understanding about the scattering analyzer through which $\Phi(\mathbf{r}_d)$ (or, more precisely, $\tilde{I}(\mathbf{r}_d)$) is measured. This can be done with a scattering matrix, and in particular the transmission sub-matrix $\mathbf{T} \equiv \mathbf{S}_{21}$. Here, $\mathbf{S}_{21}$ refers to the wave transmission sub-matrix of a 2-by-2 block-matrix formulation for the scattering matrix $\mathbf{S}$, which describes a set of incident and scattered modes. (The properties of $\mathbf{S}$ are detailed in Appendix B 1.) A plane wave basis for generating a transmission matrix is relevant for applications [6] and consistent with (although having differing character to) the mode-based [13] description or the quantum mechanical treatment of conductance channels [2, 14–17] that have been a substantial focus. Seeking insight into the experimental results from use of a random analyzer in front of a camera [1], we therefore pursue a Fourier-domain description of the speckle intensity correlation over spatial changes (translation of the diffuser or the incident field, as in the numerical simulations) in (1).

First, we draw upon the generalized Wiener-Khinchin theorem [18], which allows the normalized field correlation [12] to be written as

$$\begin{aligned} g^{(1)}(\Delta\mathbf{r};\mathbf{r}) &= \langle \tilde{\Phi}^*(\mathbf{r}_d;\mathbf{r})\tilde{\Phi}(\mathbf{r}_d;\mathbf{r}+\Delta\mathbf{r})\rangle \\ &= \frac{1}{2\pi}\int \tilde{\Phi}^*(\mathbf{k}_d;\mathbf{r})\tilde{\Phi}(\mathbf{k}_d;\mathbf{r}+\Delta\mathbf{r})e^{i\mathbf{k}_d\cdot\Delta\mathbf{r}}d\mathbf{k}_d \\ &\equiv \langle \tilde{\Phi}^*(\mathbf{k}_d;\mathbf{r})\tilde{\Phi}(\mathbf{k}_d;\mathbf{r}+\Delta\mathbf{r})\rangle, \end{aligned} \tag{2}$$

where $\tilde{\Phi}$ is the normalized field (whose coefficient of normalization differs from that of the normalized intensity $\tilde{I}$ by a square root, due to the relationship between Φ and I), $\mathbf{k}_d$ is the conjugate variable corresponding to $\mathbf{r}_d$ (the spatial variable at the detector that is evaluated at a single point in (1)), and the $\langle\cdot\rangle$ now corresponds to spectral integration and hence a sum over plane waves with randomly distributed complex coefficients.

We next discretize the plane-wave transmission matrix describing the analyzer and consider a discrete Fourier-domain representation for $\mathbf{T}$, so that we may analyze its eigenvalue decomposition using tools from random matrix theory. The vector with complex amplitudes describing the output plane wave spectrum for $\tilde{\Phi}(\mathbf{k}_d)$, using a normalization consistent with (1), is

$$\mathbf{y} = \mathbf{T}\mathbf{x}, \tag{3}$$

where $\mathbf{T}$ is the ($M \times N$ complex, non-Hermitian) transmission matrix (we will assume $M = N$), and $\mathbf{x}$ is a vector of incident plane wave coefficients with a uniformly discretized (propagating in our analysis) spectrum. We use a singular value decomposition (SVD), $\mathbf{T} = \mathbf{U}\mathbf{\Sigma}\mathbf{V}^H$, where $\mathbf{\Sigma}$ is a diagonal matrix of the singular values of $\mathbf{T}$, the matrices $\mathbf{U}$ and $\mathbf{V}$ are unitary, and ^{H} denotes the Hermitian transpose. This allows us to write the average normalized discrete (over transverse wave vector) intensity correlation in the detector half-space as

$$\begin{aligned} c_I &= \mathbf{y}_0^H\mathbf{y}_t \\ &= (\mathbf{T}\mathbf{x}_0)^H(\mathbf{T}\mathbf{x}_t) \\ &= \mathbf{x}_0^H\mathbf{T}^H\mathbf{T}\mathbf{x}_t \\ &= \mathbf{x}_0^H\left(\mathbf{V}\mathbf{\Sigma}^H\mathbf{\Sigma}\mathbf{V}^H\right)\mathbf{x}_t, \end{aligned} \tag{4}$$

where $\mathbf{y}_0$ and $\mathbf{x}_0$ contain the complex spectral amplitudes for the spatial reference position $\mathbf{r}$, and $\mathbf{y}_t$ and $\mathbf{x}_t$ those for the translated diffuser/field situation with position $\mathbf{r}+\Delta\mathbf{r}$, the unitary property of $\mathbf{U}$ has been used, and $\mathbf{\Sigma}^H\mathbf{\Sigma}$ is a diagonal matrix containing the (real, positive) eigenvalues T_n $(n = 1,\ldots,N)$ of the matrix $\mathbf{T}^H\mathbf{T}$, k of which are significant (and those close to unity most important). Discretizing the transmission matrix in this way allows us to study the continuous correlations that appear in (2) using random matrix theory.

III. FEM SIMULATION

In relation to (4), the specific nature of the eigenvalues, and the character of the random elements of $\mathbf{T}$, should dictate the characteristics of the analyzer. We pursue this point now in relation to numerical simulations, which give a solution to the sinusoidal steady state Maxwell's equations (at circular frequency, ω, corresponding to the wavelength of the light, λ) on a mesh. These FEM simulations use the arrangement in Fig 1, yielding the results summarized in Fig. 2. There, we use T to represent a random variable whose samples are T_n (after a normalization process described in Sect. IV A). The FEM solution domain, shown in Fig 1, used a scattered field formulation (so that the incident field is added to form the total field), perfectly matched layers (PMLs) on the incident and transmission sides (artificial boundaries that are highly absorbing and represent unbounded space by limiting reflections back into the domain [19]), periodic boundaries on the left and right sides, and $N = 141$ different incident plane wave directions (over ± 1.4416 rad and representing the complete propagating spectrum). The transverse wavenumbers, k_x, of these plane waves were assigned $2\pi m/L_x$, where m is an integer and L_x is the transverse period in Fig. 2, so that each is considered a mode of the periodic geometry. We used only propagating modes because the scattering slab is in the far field (regarding the small object features of interest). We note that the field solution in the analyzer is done to numerical precision and that the total field solution is Fourier transformed to form the plane wave spectrum. The analyzer is discretized into square regions of 200 nm $\times$ 200 nm, each of which is randomly assigned material (dielectric or free space) at a fill factor of 50%. The breadth is $L_x = 60$ μm and the level of scatter is controlled by thickness (L_y) of the analyzer and the dielectric constant (ϵ_r) of the filled regions, as described in the first three columns of Table I. The detector plane is a distance of 4λ from the analyzer and spans the entire breadth of the geometry (L_x). Data are collected at N points that are distributed uniformly across the detector plane, and a discrete Fourier transform is performed to calculate the elements of the matrix $\mathbf{T}$. All of these aspects of the FEM simulation are elaborated upon in Appendix A.

The transmitted field along this detector line is Fourier transformed to provide the spatial frequency complex amplitudes and hence the entries in $\mathbf{T}$. The calculated density functions of the normalized eigenvalues (of $\mathbf{T}^H\mathbf{T}$) is given in Fig. 2 for each level of scatter. This dataset includes 10 random instances of each type of scattering analyzer, and the curves became smoother as this number increased. Note the clear trend in the numerical data for increasing scatter: a larger proportion of eigenvalues near zero.

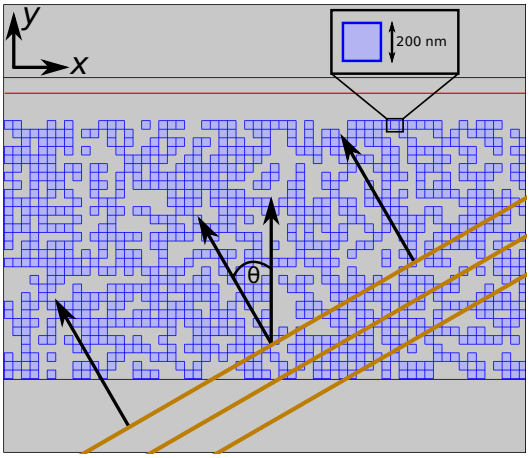

FIG. 1. The numerical simulation arrangement showing a section of a 6-μm-thick random analyzer slab (the full breadth of the slab is wider than the displayed section). The randomly populated blue squares have side lengths of 200 nm, as shown in the enlarged inset. They consist of dielectric material and have a fill fraction of 50%, while the gray region is free space. The bottom and top rectangular sections are perfectly matched layers (PMLs) in a scattered field solution. The angle (θ in the figure) of the incident plane wave (brown) was swept over ± 1.4416 rad, while the analyzer was kept stationary. The plane waves had E_z, H_x, H_y polarization, and the free-space wavelength was $\lambda = 850$ nm. The y component of the time-average Poynting vector was measured at the detector plane (red), a distance of 4λ from the top boundary of the scattering slab (this distance is not shown to scale).

The last column of Table I contains data that describes how closely the detected speckle fields satisfy the assumption of zero-mean circular Gaussian statistics that was made in Sect. II in order to form (1). If the real and imaginary parts of the electric field each follow an identical zero-mean Gaussian distribution, then the magnitude squared of the field follows a negative exponential distribution [10]. The contrast ratio (CR) of such a distribution, which is the ratio of the standard deviation to the mean of the intensity, is 1. In order to calculate these, a normally incident plane wave was shone onto each of the scattering analyzers, and the y component of the Poynting vector, S_y, was measured along the detector plane at points spaced $\lambda/100$ apart. For each such instance of each type of scattering analyzer, the mean and standard deviation of these values of S_y were calculated, and the CR calculated from these. For each type of analyzer, the 10 resulting CRs were averaged together, and these averaged results are displayed in the last column of Table I.

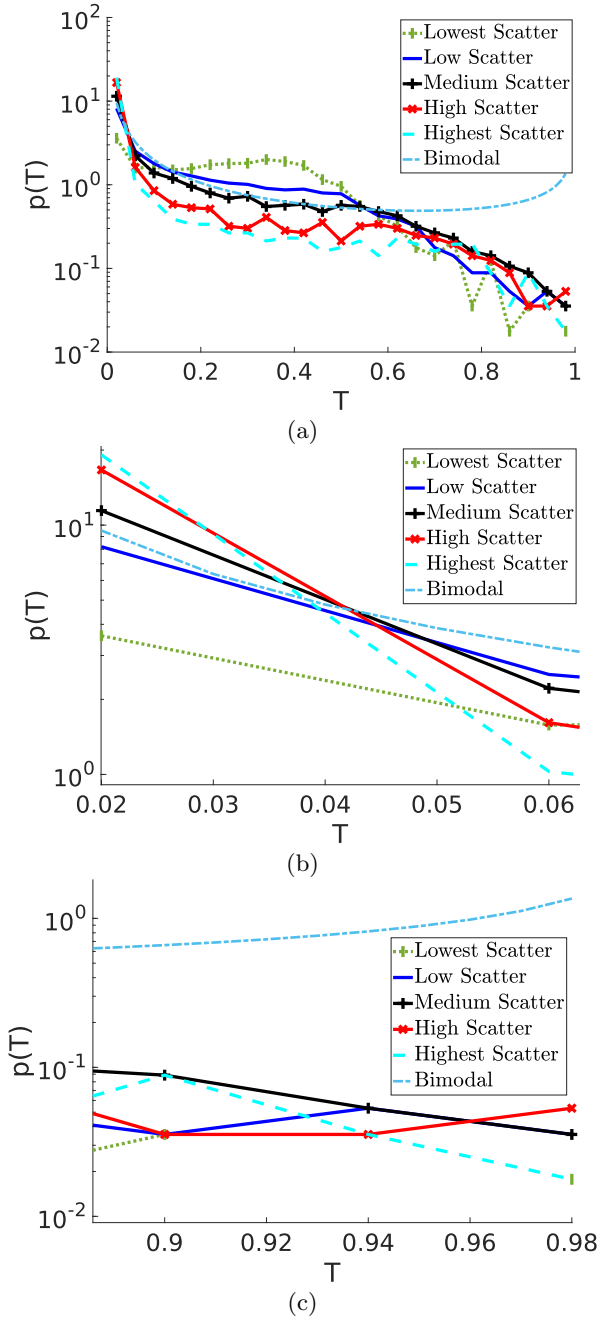

FIG. 2. (a) Empirical density functions $p(T)$ for the normalized transmission eigenvalues T of the matrix $\mathbf{T}^H\mathbf{T}$ for a plane wave spectrum with $N = 141$. Each histogram consists of 25 bins and contains 10 independently generated random instances of the scattering slabs whose configurations are listed in Table I, and is plotted with a vertical log scale. We compare these empirical probability distributions to the theoretical bimodal probability distribution in order to see if convergence occurs as the degree of scatter in the analyzer is changed. (b,c) The lower and upper ends of the plot, respectively, are shown in greater detail. The "Lowest Scatter" curve in (c) has a discontinuity: it ends at 0.9, and has a single point at 0.98. As the optical thickness of the scattering slab increases, the relative proportion of eigenvalues near $T = 0$ increases, even slightly surpassing the theoretical bimodal distribution for some configurations. No clear pattern or agreement is found for the eigenvalues near $T = 1$. Potential reasons for this are discussed in Sect. IV C 4.

TABLE I. The parameters for defining the five types of randomly scattering analyzer that were used in the numerical simulations, as well as the corresponding average speckle contrast ratios (CR).

Slab Type	Thickness L_y	Dielectric ϵ_r	CR
Lowest Scatter	1 μm	3	0.9876
Low Scatter	3 μm	3	1.0284
Medium Scatter	3 μm	5	1.0616
High Scatter	6 μm	5	1.0672
Highest Scatter	9 μm	5	1.0710

These suggest that, if the relative dielectric constant ϵ_r is too large, then increasing the analyzer thickness L_y may result in field statistics that are increasingly far from being zero-mean circular Gaussian.

IV. EIGENVALUE DISTRIBUTIONS

In this section, we introduce two theoretical eigenvalue distributions from random matrix theory: the bimodal distribution and the quarter-circle distribution. They are compared to the empirical eigenvalue distributions derived from our numerical simulations in Figs. 2 and 6, respectively. These comparisons are explored in greater detail in Sects. IV C and IV D, after a preliminary definition and calculation in Sects. IV A and IV B.

A. Normalization

The theoretical eigenvalue distributions typically appear in scaled form. However, unless special case is taken when scaling the incident plane wave amplitudes, the eigenvalues in question will not in general be limited in this way. In order to make these comparisons more appropriate, normalizations are performed.

Section IV C compares the eigenvalues of $\mathbf{T}^H\mathbf{T}$ to the bimodal distribution in Figs. 2 and 4. For these comparisons, let us define $\hat{T}_{n,m,p}$ as the nth eigenvalue of $\mathbf{T}^H_{m,p}\mathbf{T}_{m,p}$, where $\mathbf{T}_{m,p}$ is the transmission matrix of the mth ($m = 1, \ldots, 10$) random instance of a scattering analyzer with of slab type p ($p = 1, \ldots, 5$, for each row in Table I). The normalized eigenvalues T_n are derived from these $\hat{T}_{n,m,p}$ according to

$$T_n = \frac{\hat{T}_{n,m,p}}{\hat{T}_{\max}}, \tag{5}$$

where

$$\hat{T}_{\max} = \max_{n,m,p} \hat{T}_{n,m,p}.$$

By normalizing all eigenvalues from different slab types with the same scaling value, we are able to compare all of these eigenvalue distributions to one another. The

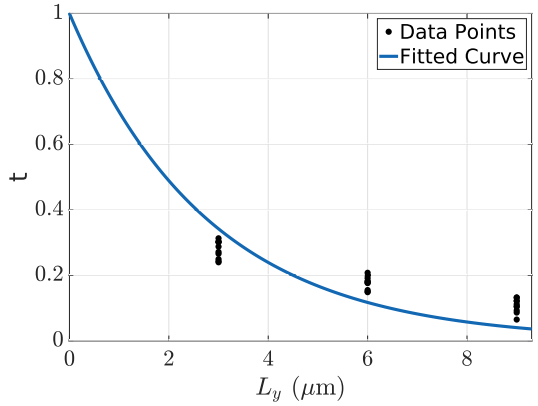

FIG. 3. Modeling the relationship between the transmission coefficient t, given in (6), the slab thickness L_y, and the mean free path ℓ, using the Beer-Lambert law. The relative dielectric constant is $\epsilon_r = 5$ for the material being modeled. The fitted curve gives an estimated value of $\hat{\ell} \approx 2.8$ μm.

resulting eigenvalues, which were always nonzero, fall in the range $T_n \in (0, 1]$. This normalization process will be implicitly assumed throughout the remainder of this work.

Section IV D similarly compares the singular values of both $\Re(\mathbf{T})$ and $\Im(\mathbf{T})$ to the quarter-circle distribution. Each of these sets of singular values is normalized using methods analogous to (5).

B. Estimated Mean Free Path Length

In order to contextualize these simulations, we use the Beer-Lambert law to estimate the mean free path length, ℓ, of the scattering material with $\epsilon_r = 5$. It relates to the transmission coefficient t and the slab thickness L_y, as [20]

$$t = e^{L_y/\ell}. \tag{6}$$

Here, t is not the normalized transmission eigenvalue T (described in Sect. IV A, and used throughout this paper), but instead the ratio of the power flowing through the detector plane to the power incident upon the slab.

The transmission coefficient t was calculated for each of the 10 instances of the Medium-, High-, and Highest-Scatter configurations (see Table I), and the exponential model in (6) was fit to the data. The results are shown in Fig. 3, and the fitted mean free path is $\hat{\ell} \approx 2.8$ μm. Except for the Lowest-Scatter configuration, all the slabs listed in Table I have a thickness $L_y \geq \hat{\ell}$.

C. Bimodal Distribution

The bimodal distribution has arisen when discussing the transmission matrix eigenvalues in scattering systems [2, 13, 21]. Prior to the appearance of an explicit form for this distribution, qualitative descriptions based on various analyses have been included in the study of conductance in one-dimensional disordered systems. Dorokhov [22] discusses a decreasing number of highly conducting states as the wire length increases, and Imry [14] gives a qualitative result based on a heuristic argument. Pendry *et al.* [23] prove what can be considered a binary approximation to the continuous bimodal distribution, showing that the transmission coefficients take on values of either 0 or 1 in the limit of increasing wire length.

The bimodal density function for T_n is given by

$$p_{\mathrm{bm}}(T) = \frac{T_0}{T\sqrt{1-T}}, \tag{7}$$

for $T \in [\delta, 1]$, δ being positive and small compared to unity, and T_0 the scaling parameter for the distribution to integrate to unity. See Appendix B for a derivation. Note that this distribution contains a non-integrable singularity at $T = 0$ (but not at $T = 1$), which is why T cannot span the full range $[0, 1]$.

The presence of this singularity makes the value of δ non-arbitrary. The peak near $T = 0$ grows larger as $\delta \to 0$, but the normalization accomplished by T_0 results in the suppression of the rest of the distribution. Therefore, as $\delta \to 0$, the peak near $T = 1$ appears to shrink relative to the peak near $T = 0$. The values of δ and T_0 are thus intertwined. The correct choice of δ corresponds to the maximum value of x in (8), discussed below in Sect IV C 4. However, because the empirical eigenvalues are being binned in a histogram, these extrema are not preserved, and this method of choosing of δ and T_0 does not result in theoretical bimodal distributions that match the empirical distributions. Choosing δ as the center of the lowest histogram bin results in the theoretical bimodal distribution curve shown in Fig. 2.

The bimodal character of (7) has been widely presented in full formality [2, 21], though this result had been in development for some time [14, 24]. It has also been investigated in relation both to waveguide problems with random scatter [13] and to statistical optics and imaging applications [3].

1. *Empirical Eigenvalue Distributions*

Figure 2 shows the empirical density functions for the normalized transmission eigenvalues T of the matrix $\mathbf{T}^H\mathbf{T}$ for a plane wave spectrum with $N = 141$. Each histogram consists of 25 bins and contains 10 independently generated random instances of the scattering slabs whose configurations are listed in Table I, and is plotted with a vertical log scale (base 10). In addition to the normalization discussed in Sect. IV A, the histograms for each slab configuration are each renormalized (this time along the vertical axis, as opposed to the horizontal axis) so that they each integrate to unity, making them valid probability distributions.

The lower and upper ends of the plot are shown with greater detail in Figs. 2(b) and (c), respectively. We compare these empirical probability distributions to the theoretical bimodal probability distribution in order to investigate trends as the degree of scatter in the analyzer is changed. No comparison is made to the quarter-circle distribution because that would be inappropriate, as is discussed in Sect. IV D 2.

Increasing analyzer scatter representative of the diffusion regime is expected to yield a bimodal density [2], a trend supported by normalized eigenvalues with a space-based $\mathbf{T}$ [25]. We find that, as the optical thickness of the scattering slab increases, the relative proportion of small eigenvalues (close to $T = 0$) increases, even slightly surpassing the theoretical bimodal distribution for some configurations, implying only moderate agreement with this theory.

No clear pattern emerges for the relatively large eigenvalues (close to 1) and the amount of scatter considered. The results also do not match the bimodal distribution, and the expected peak near $T = 1$ is not evident.

2. Statistics of the Bimodal Distribution

As a measure of the shape of $p(T)$, the bottom- and top-10% means of the normalized transmission eigenvalues are shown in Table II. These were calculated by first taking the eigenvalue sets for each random analyzer (normalized uniformly so that the maximum eigenvalue seen anywhere is 1, as detailed in the caption of Fig. 2), adding up the bottom and top 14 eigenvalues (which, out of $N = 141$ elements, corresponds to just under 10% each), and dividing each by the sum of these normalized eigenvalues. Finally, these ratios are averaged together.

Figure 2 clearly shows an increasing proportion of closed channels as the analyzer scatter increases, and the bottom-10% means in Table II agree with this trend. The top-10% means also demonstrate an increasing proportion of transmissive channels as the scatter increases, though no clear corresponding trend appears in the figure. These two patterns in Table II suggest that more agreement with the theoretical bimodal distribution may emerge as the thickness L_y is increased, despite the findings in Sect. IV B that L_y exceeds the estimated mean free path length, $\hat{\ell}$. Still, an increase in scatter is accompanied by higher proportions both of closed channels and of channels that are at least partially open, and we associate this with the demonstrated increased sensitivity to changes in the field incident on the analyzer (see Sect. V).

3. Impact of Angular Support

Here we explore the effect of reducing the angular support of the set of plane waves used in $\mathbf{T}$. Figure 4 shows the effects of using different subsets of central modes (the lowest-order modes, whose k_x is close to zero), with the Highest Scatter slab type (Table I). Interestingly, reducing this set of plane waves seems to have a somewhat similar effect on the eigenvalue distribution as reducing the amount of scatter in the analyzer: the peak near zero shrinks in height. However, no trend appears near $T = 1$.

TABLE II. The bottom- and top-10% means of the normalized transmission eigenvalues, for the bimodal distribution. This data agrees with the model's argument that, as the level of scatter increases in the analyzer, the eigenvalue distribution becomes more bimodal (even though this trend can be only partially found in Fig. 2).

Slab Type	Bottom 10%	Top 10%
Lowest Scatter	2.5959×10^{-3}	0.2301
Low Scatter	3.6097×10^{-4}	0.3203
Medium Scatter	7.1288×10^{-5}	0.3936
High Scatter	2.1257×10^{-6}	0.5791
Highest Scatter	1.4675×10^{-7}	0.7235

4. Assumptions of the Bimodal Distribution

For further insight into potential reasons for the absence of the high-eigenvalue peak in Fig. 2, we turn to the derivation [2] of the bimodal distribution. Appendix B has the relevant background details and derivations. One important assumption involves the values x_n, which are related to the eigenvalues T_n that appear in (7) by

$$T = \frac{1}{\cosh^2 x}, \tag{8}$$

or

$$x = \cosh^{-1}\left(\frac{1}{\sqrt{T}}\right), \tag{9}$$

where x is a random variable of which x_n are samples (similar to the relationship between T and T_n). Note that x breaks with the convention used elsewhere throughout this paper that random variables are represented using capital letters. This notation is used here in keeping with existing literature.

It has been noted that, for the scattering regime where the bimodal distribution is an appropriate model for the transmission eigenvalues, the probability distribution for x_n tends towards uniform [2, 17]. Indeed, such uniformity forms a basis for the derivation of the bimodal distribution (7), as shown in Appendix B. We therefore apply the transformation defined in (9) to the values of T_n that are plotted in Fig. 2. The resulting x_n are compared to a uniform distribution in Fig. 5.

Figure 5 shows that these x_n are not in fact uniformly distributed, meaning that the scattering regime resulting from our simulations is not the same as the one in which we would expect to see a bimodal eigenvalue distribution. This explains the absence of the high-eigenvalue peak in

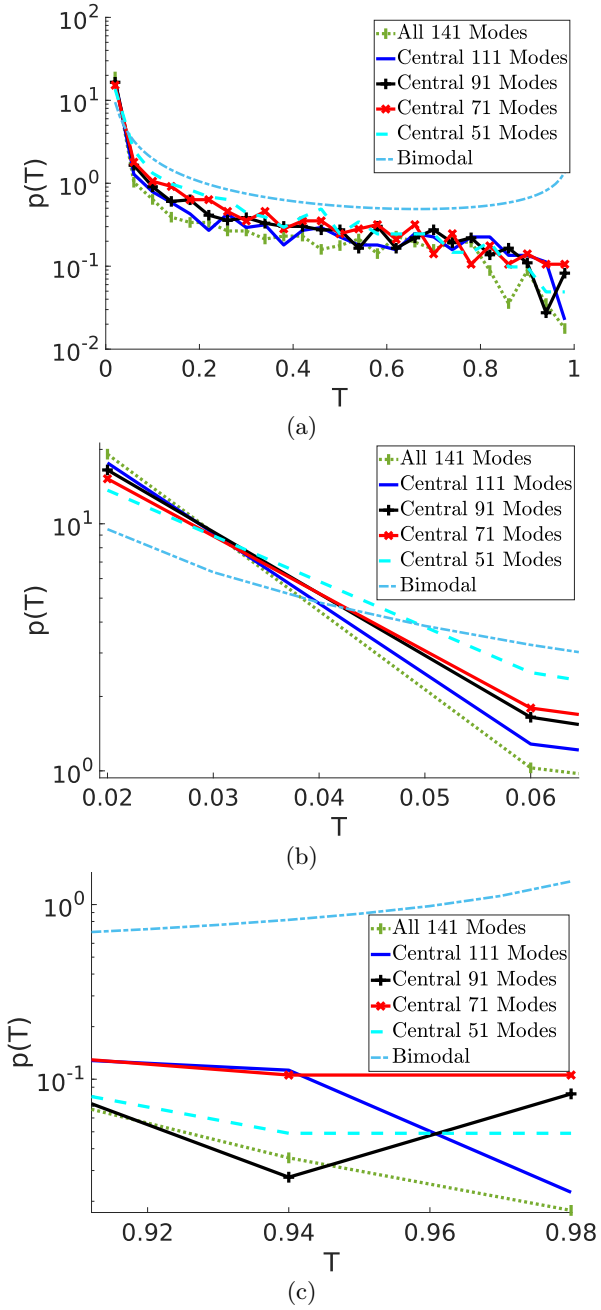

FIG. 4. Comparison of empirical density functions for the normalized transmission eigenvalues T from the SVD of $\mathbf{T}^H\mathbf{T}$ for different amounts of angular support in the set of incident plane-wave modes. Only the Highest Scatter slab type (described in Table I) was used. Only the "central" angles were kept, meaning those whose angles of incidence were close to normal with respect to the slab. (a) The data here was taken from the same simulations that were used to generate Fig. 2, and was processed similarly. The bimodal probability distribution is also shown, for comparison. (b,c) The lower and upper ends of the plot, respectively, are shown in greater detail. Note that, as the set of incident plane waves becomes less complete (with respect to the set of propagating modes), the relative proportion of small eigenvalues (close to 0) decreases. No clear relationship emerges between the number of modes used and the relative proportion of large eigenvalues.

Fig. 2. However, the curves do appear to approach the uniform distribution as the amount of scatter increases, when looking at the region $x_n > 5$. On the other hand, such a relationship does not exist for the other notable region, around $x_n < 2$. In fact, this behavior is analogous to that of Fig. 2: the low-eigenvalue peak grows higher as the amount of scatter increases, while the high-eigenvalue peak does not. The relationship between these two figures is not coincidental. Equation (9) is strictly monotonically decreasing for $T_n \in (0, 1)$, which is the range of T_n plotted in Fig. 2. Therefore, the left side of Fig. 5 is related to the right side of Fig. 2(a), and vice versa. For this reason, the normalization procedure performed on T_n (Sect. IV A) may play a role in the steep feature around $x_n < 2$.

These results suggest that we may expect the lower peak of the bimodal eigenvalue distribution in Fig. 2 to continue to be better represented as the amount of scatter in the analyzer is increased. While the upper peak has not appeared for the types of scattering slab used in this paper, the results of Sect. IV C 2 suggest that both peaks may grow as the amount of scatter is further increased. While the assumption does not hold that the scatterers are far apart compared to the wavelength, this is unlikely to be the cause for the lack of an upper peak, as the CRs in Table I are close to unity. The relatively low number of eigenvalues near $T = 1$ means that statistical convergence in this region may not have been achieved. It has been suggested using an incomplete set of channels when calculating the transmission matrix could cause this $T = 1$ peak to fail to appear [13], though our simulations use the full set of propagating plane-wave

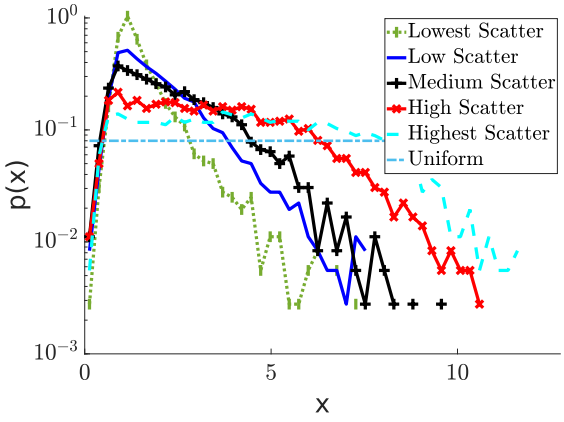

FIG. 5. Density functions for the x calculated from the empirical distributions of T that are shown in Fig. 2, using (9). The histograms were calculated in a similar method to those in Fig. 2, except that 50 bins were used instead of 25. They are not uniform distributions, thus indicating that the scattering regime resulting from our simulations is not the same as the one in which we would expect to see a bimodal eigenvalue distribution, but the trend towards uniform as scatter increases is clear. This explains the absence of the high-eigenvalue peak in Fig. 2.

modes. However, there are differences between our simulations and those of Goetschy and Stone [13]. For one, the contrast between the regions of high ϵ_r and low ϵ_r within the scattering medium is higher in our simulations than in theirs. Also, their scattering medium was about twice as large (relative to the wavelength λ) as our largest slab, in both dimensions. It also had a slightly different structure, having less of a difference between regions of high and low dielectric constant. As a result, they had over thrice our number of eigenvalues ($N = 485$ versus $N = 141$). Their findings indicate a certain sensitivity of the presence of this high-eigenvalue peak to the simulation parameters, and the same explanation holds here regarding the bimodal eigenvalue distribution.

D. Quarter-Circle Distribution

We now turn our attention to a different eigenvalue distribution. While the bimodal distribution arose from a physical background, the quarter-circle distribution originated from random matrix theory. Specifically, it first appeared during a derivation by Wigner of the eigenvalue distribution of random-sign real symmetric matrices [26]. This class of matrices was generalized in later work [27], allowing the distribution to be applied to real symmetric Gaussian matrices.

Wigner's research was further extended by Marčenko and Pastur in several ways, notably allowing for complex-valued matrices [28]. The constraints on the properties of the random matrix for this eigenvalue distribution to be valid have been loosened over time. We will simply note here that they are satisfied by independent and Gaussian-distributed matrix elements, but a more thorough review of the history of the quarter-circle distribution and its assumptions can be found in Appendix C. The simplified quarter-circle density function that we use, with $\sigma \in [0, 1]$, is

$$p_{\mathrm{qc}}(\sigma) = \frac{4}{\pi}\sqrt{1-\sigma^2}, \tag{10}$$

where σ is a random variable corresponding to the eigenvalues of the appropriate random matrix. We have so far been studying the eigenvalues of the random matrix $\mathbf{T}^H\mathbf{T}$, since they relate to the correlation data, as presented in (4). When studying the quarter-circle distribution though, we consider the field transmission matrix $\mathbf{T}$. We also consider its singular values, rather than its eigenvalues, as is explained next.

1. Empirical Singular Value Distributions

While the work by Marčenko and Pastur shows that complex-valued random matrices can have quarter-circle-distributed eigenvalue distributions, the assumptions made in their derivation are somewhat unclear in our context. As detailed in Appendix C, they all refer to properties of the random matrix that are more formal than what we have access to. Therefore, rather than investigating the complex-valued matrix $\mathbf{T}^H\mathbf{T}$, we will instead use the real-valued matrices $\Re(\mathbf{T})$ and $\Im(\mathbf{T})$ (the real and imaginary parts of $\mathbf{T}$, respectively). These matrices are not symmetric, so their eigenvalues are complex in general. Instead, the (real-valued) singular value distributions of these matrices are compared to the quarter-circle distribution in Fig. 6. The singular values (normalized as described in Sect. IV A) of $\Re(\mathbf{T})$ and $\Im(\mathbf{T})$ are σ_R and σ_I, respectively. The decision to compare these matrices' singular value distributions to the quarter-circle distribution is not merely a practical one: it is actually the more correct choice of comparison in a rigorous sense.

By reviewing the details of the quarter-circle distribution more closely (see Appendix C), we note that the matrix $\mathbf{T}$ already satisfies one of the distribution's requirements. In forming (1), we required the detected fields (and hence the entries in $\mathbf{T}$) to be zero-mean circular Gaussian. That is, both the real and imaginary parts of $\mathbf{T}$ ($\Re(\mathbf{T})$ and $\Im(\mathbf{T})$, respectively) have been assumed to have zero-mean Gaussian statistics.

If these matrix entries are independently distributed as well, then the only remaining constraint [27] required for the eigenvalues (singular values) to follow a quarter-circle distribution is for these two matrices to be symmetric. For example, if such independence were to exist, then the matrices $\Re(\mathbf{T}) + \Re(\mathbf{T})^\top$ and $\Im(\mathbf{T}) + \Im(\mathbf{T})^\top$ (where $^\top$ represents the transpose) would be expected to have eigenvalue distributions that follow the quarter-circle distribution. Indeed, the quarter-circle distribution has been found experimentally when studying the singular value distribution of transmission matrices for disordered media [3]. However, it will now be shown that such assumptions on $\mathbf{T}$ are incompatible with the matrix $\mathbf{T}^H\mathbf{T}$ having a quarter-circle eigenvalue distribution.

2. Applicability of the Quarter-Circle Distribution

This section demonstrates that the matrices $\mathbf{T}$ and $\mathbf{T}^H\mathbf{T}$ cannot simultaneously satisfy the assumptions of the quarter-circle distribution. This is done by assuming the statistics of $\mathbf{T}$ and proving that the diagonal elements of $\mathbf{T}^H\mathbf{T}$ are distributed according to an Erlang distribution (which is related to the χ^2 or chi-square distribution), rather than the required exponential distribution.

The Erlang and χ^2 distributions [29] are both special cases of the Gamma distribution. The Erlang distribution with shape parameter k and rate parameter γ has the density function

$$f_{\mathrm{Er}}(x; k, \gamma) = \begin{cases} \frac{\gamma^k x^{k-1}}{(k-1)!} e^{-\gamma x} & x \geq 0 \\ 0 & \text{otherwise,} \end{cases} \tag{11}$$

while the χ^2 distribution with k degrees of freedom (de-

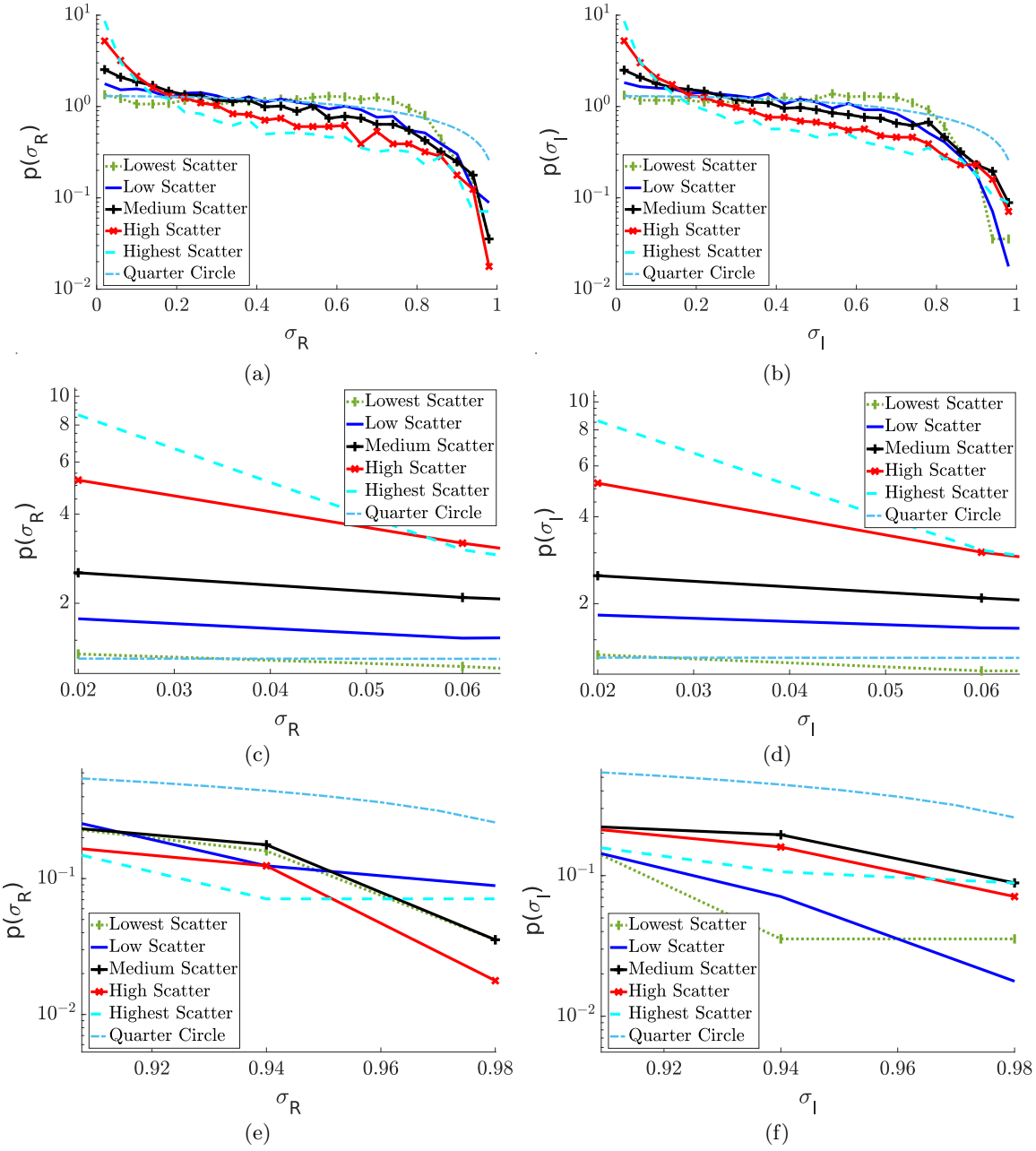

FIG. 6. Density functions for the normalized singular values of the matrices (a,c,e) $\Re(\mathbf{T})$ and (b,d,f) $\Im(\mathbf{T})$ for a plane wave spectrum with $N = 141$. The data here was taken from the same simulations that were used to generate Fig. 2, and was processed in a similar way. Subfigures (a) and (b) show probability distributions corresponding to $\Re(\mathbf{T})$ and $\Im(\mathbf{T})$, respectively. Subfigures (c) and (e) show the lower and upper ends, respectively, of (a) in greater detail. Subfigures (d) and (f) correspond to (b) in the same way. The theoretical quarter-circle distribution is included for comparison, and good agreement with it is found. This is somewhat surprising, as symmetry is a requirement for quarter-circle statistics, (as discussed in Sect IV D), and the matrices $\Re(\mathbf{T})$ and $\Im(\mathbf{T})$ are not symmetric, nor are their entries independently distributed. This may explain why the empirical distributions, compared to the quarter-circle distribution, tend to have more eigenvalues close to 0, and fewer eigenvalues close to 1.

noted χ^2_k) has the density function

$$f_{\chi^2}(x;k) = \begin{cases} \frac{x^{n/2-1}}{2^{n/2}\Gamma(n/2)} e^{-x/2} & x \geq 0 \\ 0 & \text{otherwise.} \end{cases} \tag{12}$$

The connection between the Erlang and χ^2 distributions is interesting. Comparing (11) and (12), we note that an Erlang distribution with rate parameter $\gamma = 1/2$ and shape parameter $k = n/2$ is equivalent to a χ^2 distribution with k degrees of freedom.

Next, it can be shown [29] that, given n independent

Gaussian random variables z_i with zero mean and unit variance, their sum of squares $\sum_{i=1}^{n} z_i^2$ follows a χ^2 distribution with n degrees of freedom. Taken with the previous result, this means that, if the number of such Gaussian random variables n is even, then this sum follows an Erlang distribution with shape parameter $k = n/2$ (and rate parameter $\gamma = 1/2$).

Now, the matrix $\mathbf{T}^H\mathbf{T}$ is in general complex-valued (with Hermitian symmetry), except for the diagonal elements, which are real-valued. If $\mathbf{T}^H\mathbf{T}$ is an $N \times N$ matrix, then the ith element along its diagonal is given by

$$\left(\mathbf{T}^H\mathbf{T}\right)_{ii} = \sum_{j=1}^{N} \Re(\mathbf{T}_{i,j})^2 + \Im(\mathbf{T}_{i,j})^2. \tag{13}$$

Therefore, if the elements of $\mathbf{T}$ are independently distributed zero-mean Gaussian random variables, then the diagonal elements of $\mathbf{T}^H\mathbf{T}$ follow a χ^2_{2N} distribution, which is equivalent to an Erlang$(N, 1/2)$ distribution. Regardless of the behavior of the (complex-valued) off-diagonal matrix elements, these diagonals prevent $\mathbf{T}^H\mathbf{T}$ from satisfying the requirements for its eigenvalues to follow a quarter-circle distribution.

Still, the statistics resulting from (13) do hold a certain conceptual similarity with those mentioned in Sect II. Zero-mean circular Gaussian field statistics result in intensity statistics that follow an exponential distribution (sometimes called negative exponential [10]), which has the distribution [29]

$$f_{Ex}(x;\gamma) = \gamma e^{-\gamma x}, \tag{14}$$

where γ is the rate parameter. By comparing (11) and (14), we see that the exponential distribution is merely a special case of the Erlang distribution, with shape parameter $k = 1$. This means that, if we were to let $N = 1$ in (13) (corresponding to a single plane wave and a single measurement), then we would indeed have negative-exponential statistics in $\mathbf{T}^H\mathbf{T}$, resulting in an albeit trivial case of a quarter-circle-distributed eigenvalue.

3. Statistics of the Quarter-Circle Distribution

Section IV D 2 mentioned the conditions required of a random matrix for its eigenvalues to follow the quarter-circle distribution. Here we examine how closely these are met.

One condition on the matrix entries is that they must be independently distributed [27] (except for the symmetry of the matrix). We will use the distance correlation [30] between pairwise matrix elements of some matrix $\mathbf{A}$ to measure this independence. For reasons discussed above, $\mathbf{A} = \Re(\mathbf{T})$ and $\mathbf{A} = \Im(\mathbf{T})$ will be examined, and the results displayed in Table III. For this analysis, each matrix element $\mathbf{A}_{i,j}$ is considered a random variable, where $i, j \in \{1, \ldots, 141\}$. For each type of scattering slab, any given random variable $\mathbf{A}_{i,j}$ can be said to have been sampled 10 times, as that is the number of slab instances of each type that were numerically generated. For any pair $\mathbf{A}_{i,j}$ and $\mathbf{A}_{i',j'}$, their distance correlation can be computed as a measure of independence. The resulting average distance correlations were thus calculated [31] and are shown in Table III. Note that the distance correlation between two random variables is 0 if and only if they are independent. The results indicate that the matrix elements are not independent, and do not approach independence for the slabs that we have simulated.

TABLE III. Statistics of the $\mathbf{T}$ matrix elements resulting from the numerical simulations: mean distance correlation (Dist. Corr.) and mean contrast ratio (CR). These values indicate how independently distributed they are and how Gaussian-distributed they are, respectively. Both of these properties relate to the quarter-circle distribution.

Slab Type	Dist. Corr.		CR
	$\Re(\mathbf{T})$	$\Im(\mathbf{T})$	$\mathbf{T}$
Lowest Scatter	0.5044	0.5048	0.9876
Low Scatter	0.5045	0.5043	1.0284
Medium Scatter	0.5043	0.5049	1.0616
High Scatter	0.5050	0.5047	1.0672
Highest Scatter	0.5056	0.5050	1.0710

The final column of Table III contains the mean contrast ratios (CRs) for the complex elements of the matrix $\mathbf{T}$, which were also displayed in Table I. As discussed in Sect. III, a mean CR near 1 is an indicator that the field follows a zero-mean circular Gaussian distribution. These statistics are repeated here in order to gauge how closely the elements of the real-valued matrices $\Re(\mathbf{T})$ and $\Im(\mathbf{T})$ each follow zero-mean Gaussian distributions with identical variances. These same statistics therefore appear in two different contexts throughout this work. As a result, we would expect that, as the field more closely approaches zero-mean circular Gaussian statistics, the eigenvalues of the matrices $\Re(\mathbf{T})$ and $\Im(\mathbf{T})$ more closely approach a quarter-circle distribution.

Still, it should be noted that an assumption of zero-mean circular Gaussian field statistics was made in forming (1) only because of the basis of a moment theorem used to relate intensity and field correlations. However, the discrete mathematical description in Sect. II involving field correlations over space, notably (4) and the ensuing treatment of $\mathbf{T}^H\mathbf{T}$, does not require Gaussian properties and remains valid regardless of the field statistics.

V. SUPER-RESOLUTION FAR-FIELD SENSITIVITY

We have previously established [1], with experimental and simulation-based data, that the use of a randomly scattering analyzer can enhance subwavelength sensitivity to either a shifting incident electric field or a changing

field associated with a remote shifting object. This section elaborates upon that result by demonstrating super-resolution sensitivity in a fundamental way: distinguishing between two features that are separated in space by a subwavelength distance.

A. Super-Resolution Far-Field Simulation

The object's features take the form of two apertures in a 200-nm-thick perfect electric conductor (PEC) film that otherwise spans the entire breadth of the geometry, as illustrated in Fig. 7. A small central PEC segment is added or removed, creating either one large aperture or two smaller apertures in the PEC. The PEC plane is placed below the analyzer slab (see Fig. 1), so that the incident field has to pass through the apertures before reaching the analyzer. There is a free-space margin of 2λ between the PEC and the bottom PML (for numerical purposes). There is also a gap of 2λ between the PEC and the bottom of the analyzer slab. For each of the configurations in Table I, 10 different random analyzer slabs were generated (except for the Highest Scatter case, which required more memory than was available on our compute server); the resulting correlations were averaged together. We also compare to a "control" case, in which no random analyzer is present at all. The correlation curves shown in Fig. 8 were calculated as described in Appendix A 5.

It should be noted that, since the aperture construction has a total size of λ, the far-field distance is approximately $2(\lambda)^2/\lambda = 2\lambda$ away. Because this is in fact the distance between the aperture construction and analyzer slab (when applicable), this analyzer can be considered a far-field sensing system.

The correlations plotted in Fig. 8 were calculated over the changing detected speckle intensity patterns that resulted from translating the aperture system shown in Fig. 7 through a normally-incident plane-wave background field. Specifically, the aperture system is translated in intervals of $\lambda/10$, up to a maximum of $\lambda/2$ in each direction ($+x$ and $-x$). This contrasts with our previous work [1], in which the detected speckle intensity patterns change in response to a translating (randomly generated) background speckle field, with everything else being stationary. Here, the translating apertures render it unnecessary to have a shifting speckle field, or to even have a stationary one, which is why we switch to using a simple normally incident plane wave. This has the added benefit of eliminating one of the sources of randomness in the simulations (the other being the distribution of random scatterer positions in the analyzer, which still remains). This improves the distinguishability between the one-aperture and two-aperture cases by effectively removing what can be thought of as a source of noise.

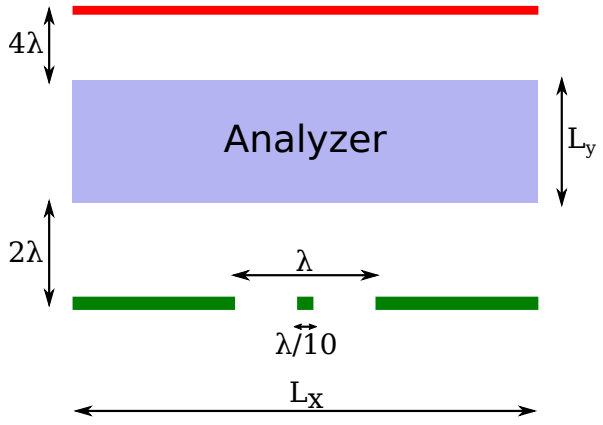

FIG. 7. Diagram of two apertures in a 200-nm-thick PEC film (green). This is placed 2λ in front of the analyzer (blue) in order to demonstrate super-resolution sensitivity to the absence or presence of the central PEC segment ($\lambda/10$ across). When this central segment is removed, the single remaining aperture has a width of λ. The PEC otherwise spans the entire breadth of the geometry, L_x. As in Fig. 1, there is a separation of 4λ between the analyzer and the detectors.

B. Speckle Intensity Correlations

Figure 8 exhibits several patterns. Without a scattering analyzer, the one-aperture and two-aperture cases are difficult to distinguish. When a scattering analyzer is added, the decorrelation curves become more distinguishable. This demonstrates far-field super-resolution sensing.

It should be noted that, while the one-aperture and two-aperture curves in the No Analyzer case are separated by much less than when an analyzer is present, the mere presence of any separation at all may suggest the possibility of such super-resolution sensing without an analyzer (albeit with less effectiveness). However, noise has been neglected. Out interest here is in enhancing the separation of the two object cases, which indicates an ability to distinguish them in a noisy environment. The key point is that sensitivity is enhanced by the analyzer.

1. *Using Standard Slab Types*

We began by using the same types of scattering analyzer that are parameterized in Table I (except for the Highest Scatter type, which our computer had insufficient memory to simulate), with $\epsilon_r \in \{3, 5\}$. Some expected patterns are noticeably absent from Figs. 8(a) and (c) for this situation. For the Lowest Scatter and Low Scatter analyzer types, an increase in scatter results in a faster decorrelation as well as greater separation between the one-aperture and two-aperture curves. This increases sensitivity, and it reinforces prior results [1] (even though we have used a plane-wave illumination in this work, rather than the speckle-field illumination of

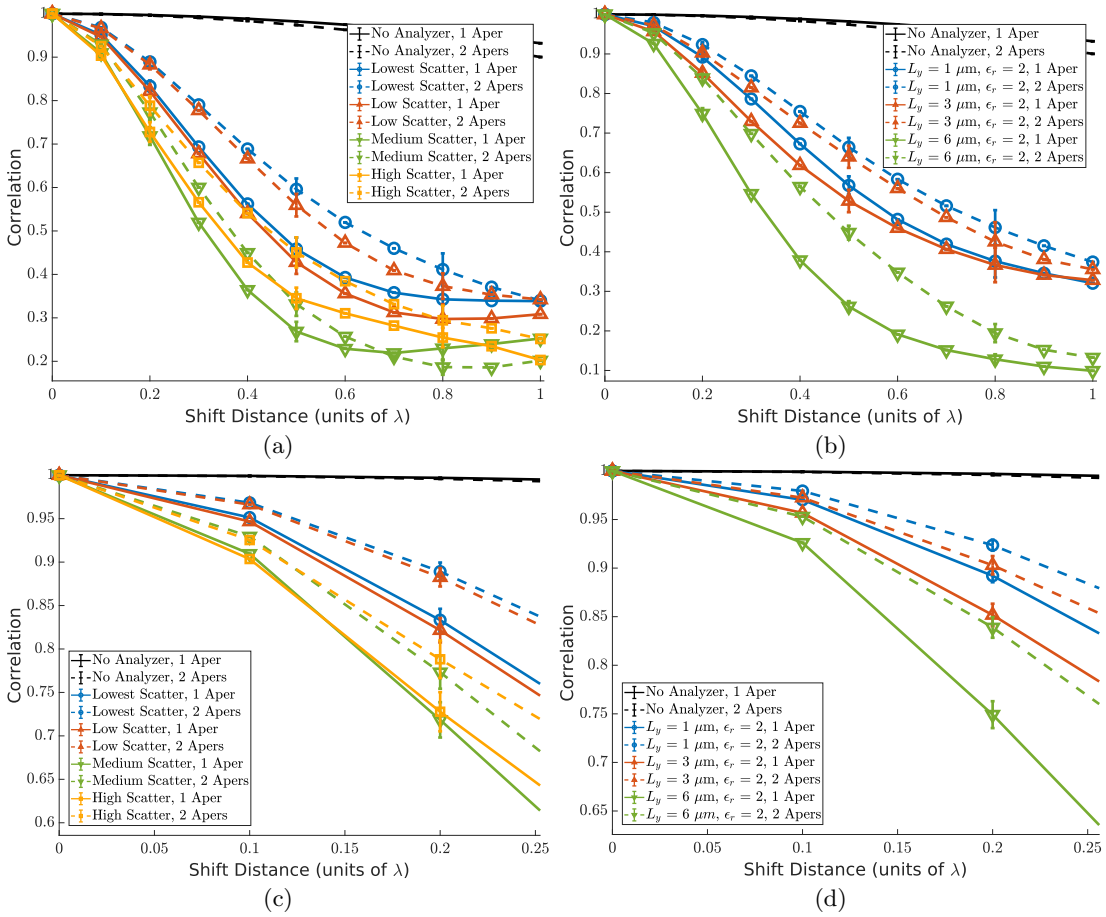

FIG. 8. Correlations over shifting aperture(s), illuminated by a normally incident plane wave, with or without an analyzer slab. The different colors each represent a different type of analyzer (or lack thereof). The solid lines represent one aperture, while the dashed lines represent two apertures. Error bars are shown based on averaging the results of 10 different random analyzers (where applicable). While the difference between the one-aperture and two-aperture setup is difficult to distinguish in the absence of an analyzer slab, they become more distinguishable with the addition of a scattering random analyzer. This demonstrates far-field super-resolution sensing. (a,c) The same types of analyzer from Table I are used. Surprisingly, increasing the amount of scatter does not consistently result in faster decorrelation and greater separation (sensitivity). (b,d) After lowering the dielectric constant to $\epsilon_r = 2$, this pattern indeed holds.

the previous work). However, the Medium Scatter and High Scatter do not follow this pattern. By consulting Table I, we notice that this change comes about with the transition from $\epsilon_r = 3$ to $\epsilon_r = 5$.

2. *Reduced Dielectric Constant*

Exploring this lack of a consistent trend, we also tried simulating analyzers with a lower dielectric constant, $\epsilon_r = 2$, with the results in Figs. 8(b,d). When using $\epsilon_r = 2$, a more complete pattern emerges: by increasing the thickness of the scattering analyzer (and therefore increasing the amount of scatter), the speckle decorrelates more quickly, and there is a greater difference between the one-aperture and two-aperture decorrelation curves, thereby resulting in greater sensitivity. This suggests that increasing the thickness of a randomly scattering analyzer, rather than the dielectric constant, may be a preferable method of increasing far-field subwavelength sensitivity.

C. Object Function Comparison

Figure 8 shows that, for the no-analyzer case, the two-aperture correlation decays slightly more quickly than the one-aperture correlation. This can be understood by considering the Fourier transform of the object function (aperture arrangement), which gives an approximation for its effect in the far field. Here, the object function is being used as a proxy for the fields that lie within the aperture(s). The far-field approximation of a compact source or field distribution can be written in terms of the spatial Fourier transform of the source distribution, regardless of position. This vector field result requires the

distance to the detector points be large relative to both the wavelength and the source size, hence the size of the effective source in wavelengths is relevant. In our case, we have a periodic transverse arrangement, where the period is very large compared to the wavelength. With a small aperture and a relatively large spatial period, we can move into the far field of the aperture at a distance that is still much less than the period. If the object function is nonzero where the apertures exist, then (ignoring the periodic boundary conditions) the object functions are estimated as

$$o_1(x) = \text{rect}\left(\frac{x}{\lambda}\right)$$

and

$$o_2(x) = \text{rect}\left(\frac{x}{\lambda}\right) - \text{rect}\left(\frac{x}{\lambda/10}\right)$$

for the one-aperture and two-aperture case, respectively, where $\text{rect}(x)$ is a rectangle function of unit width. We have thus assumed that the field has constant amplitude across the aperture (generally used as an approximation when the aperture is large compared to the wavelength and with a normal plane wave incident), but here applied to a small aperture for qualitative insight. The Fourier transforms of these object functions are

$$O_1(k_x) = \lambda\ \text{sinc}\left(\frac{\lambda k_x}{2}\right) \tag{15}$$

and

$$O_2(k_x) = \lambda\ \text{sinc}\left(\frac{\lambda k_x}{2}\right) - \frac{\lambda}{10}\ \text{sinc}\left(\frac{\lambda}{10}\frac{k_x}{2}\right), \tag{16}$$

for $\text{sinc}(k_x) = \sin(k_x)/k_x$. Comparing (15) and (16), we see that the addition of the small PEC segment (Fig. 7) in the two-aperture case slightly narrows the far-field aperture response, as shown in Fig. 9(a). The autocorrelation functions are very similar in Fig. 9(b), though this is a slightly different metric than the method based on the Pearson correlation coefficient, which is used to generate Fig. 8 and is detailed in Appendix A 5.

We note that the decorrelation rate order in Fig. 8 appears to reverse when a scattering analyzer is added: the one-aperture correlation decays faster than the two-aperture correlation. This might be expected given earlier experimental work involving extraction of the (patterned) field incident on a randomly scattering slab from speckle intensity correlations over position [32, 33]. It was found that a larger object (circular apertures in a screen with greater separation in this case), having a narrower spatial Fourier transform (far field distribution), resulted in a slower decorrelation with measurements through a randomly scattering slab [32]. The basic understanding from this earlier work, with translated patterned fields incident on a random medium and measured intensity speckle correlations over translated position, is that the Fourier magnitude of the incident field spectrum (from the object) is being accessed (and the incident field could thus be determined with phase retrieval). In the cases considered here, the double aperture system in Fig. 7 has the narrower Fourier transform (Fig. 9) and also the slower decorrelation in Fig. 8, with use of the analyzer. As the aperture system is translated, the total field is changed everywhere. This means that the situation is not exactly as in Ref. [32], where a remote (at a substantial distance) beam was patterned and sensed through a scattering medium, yet the conclusions on the influence of the aperture system (where that with a narrower far-field or source spatial Fourier transform has the faster decorrelation) are similar. Our results in Fig. 8 could thus be interpreted as providing access to certain features of the two different object functions (of the aperture systems) even amid the continual changes in the total field. However, and of significance here, the motion effect and the changing fields sensed by the analyzer provides access to subwavelength object information.

D. Speckle Intensity Statistics and Scattering Regime

The speckle intensity patterns that were attained in Sect. V A are now inspected further. One possible scattering regime results in zero-mean circular Gaussian speckle intensity statistics, as is discussed in Sect. II. Such statistics are marked by an intensity CR that is close to unity. With plane wave illumination of the object, the resulting CRs obtained at the detector plane, shown in Table IV, are not close to unity. When compared to the CRs in the last column of Table I (which are much closer to unity), these indicate that introduction of a PEC film with a small aperture(s) has dramatically changed the field statistics.

When the speckle intensity pattern is examined, an intensity envelope is clearly noticeable, indicating a lack of uniform intensity statistics. The envelope's width is considerably larger than the distance over which the correlations in Fig. 8 are calculated (the first slab of the High Scatter type has a full width of about 30 μm, or about 35λ), meaning that this envelope plays only a negligible direct role in the decorrelations. It is also clear that the level of scatter in the analyzers used here was not high enough to generate zero-mean circular Gaussian field statistics that are stationary across the entire breadth of the detector plane, despite the findings in Sect. IV B that almost all the slab types studied in this paper have a thickness, L_y, of at least one mean free path length, ℓ.

All previous experimental work involving coherent light passing through a heavily scattering medium [1, 8, 32, 33], though, has had sufficient scatter to achieve unit CRs, thereby indicating the presence of such statistics. Because the results presented here are in a different statistical regime as previous experimental results, being neither uniform nor zero-mean circular Gaussian, we

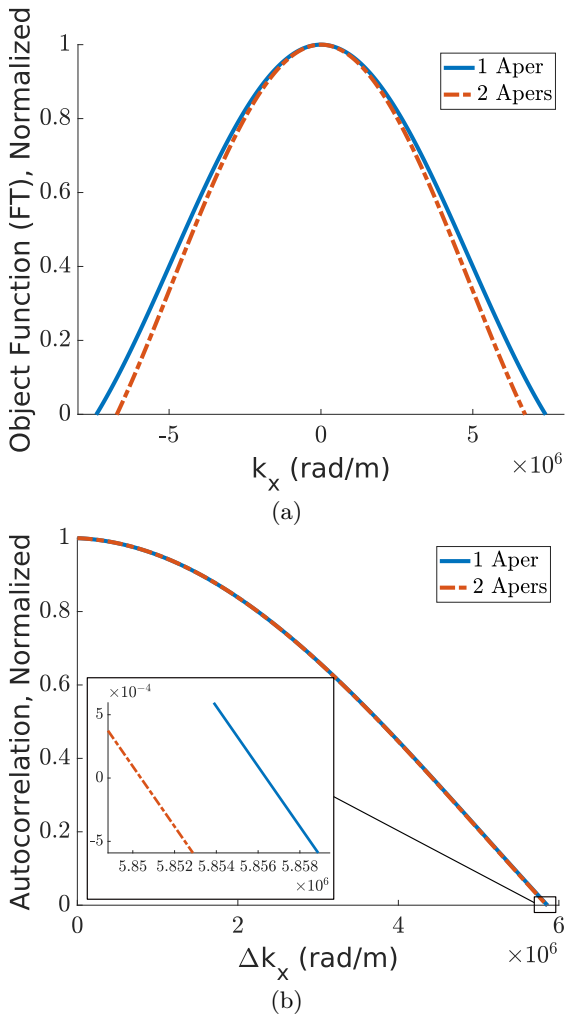

FIG. 9. (a) Fourier transforms of the object functions for the one-aperture case and two-aperture case, (15) and (16), respectively. These transforms were then both normalized to maximum values of one. Only the main lobes of these sinc functions are shown here, though the side ripples do exist. Note that the two-aperture case results in a slightly narrower far-field aperture response. This is why, for the no-analyzer case in Fig. 8, the two-aperture case decorrelates slightly faster than the one-aperture case. (b) Autocorrelations of the object function Fourier transforms, again normalized to unit maxima. They are very difficult to distinguish, and the inset shows how close the zero-crossings are. This similarity demonstrates the power of the random analyzer to increase sensitivity.

should not expect full agreement with all of their conclusions. Still, cross-referencing Table IV with Fig. 8 suggests that such statistics might be achieved by increasing the thickness L_y while possibly decreasing the dielectric constant ϵ_r. This should also enlarge the intensity envelope, making the statistics more uniform. Notably, these statistics show that the results presented herein extend beyond previous work [1]: super-resolution far-field sensitivity (Sect. V A) to a subwavelength change is not limited to one particular type of field statistics, i.e., zero-mean circular Gaussian fields.

E. Proposed Explanation

An explanation for the presented super-resolution results is proposed here, though further exploration is needed to test parts of it. Because the object and analyzer are outside the near-field region of each other, practical sensing will not be based on the evanescent portion of the plane wave spectrum for the field scattered by the object. With a measure such as the illumination domain, or in the numerical problem treated with a periodic boundary condition (or equivalently, in some waveguide arrangement), the incident mode will scatter from the analyzer and generate speckle. In this situation, the object (the aperture system) is translated in this background field, and it is the change in the total field (background plus the scattered field due to the object) that the analyzer senses. In this manner, far-subwavelength object information can be encoded from the near field into the propagating spectrum, as has been previously demonstrated using object motion in structured illumination [9].

This propagating spectrum is sampled by the random analyzer. The modes each excite the eigenchannels of the analyzer slab, and are weighted by the corresponding eigenvalues. In the extreme case of a completely uniform eigenvalue distribution (all eigenchannels open, corresponding to no analyzer), any change in one or more of the incident field modes will be averaged together with all other modes. As the eigenvalue distribution becomes more selective though (fewer open eigenchannels, corre-

TABLE IV. Speckle intensity statistics for the simulations in Sect. V A. These differ from the statistics in Table I because of the aperture(s) in the PEC. As discussed in Sect. II, a speckle contrast ratio near unity indicates zero-mean circular Gaussian field statistics. CRs were calculated for each of the random analyzers used in generating Fig. 8, and were then averaged together. The CR is not applicable for the No Analyzer case, because no speckle field is expected. In a pattern similar to Fig. 8, increasing L_y while keeping $\epsilon_r = 2$ results in statistics that more reliably converge to unity than increasing both L_y and ϵ_r. This suggests a connection between the statistics of the speckle and the far-field sensitivity of the analyzer.

	Contrast Ratio	
Slab Type	1 Aperture	2 Apertures
No Analyzer	N/A	N/A
Lowest Scatter	2.3196	2.2086
Low Scatter	1.9389	1.9627
Medium Scatter	1.9795	1.9833
High Scatter	1.4852	1.5582
$L_y = 1$ μm, $\epsilon_r = 2$	2.3077	2.5385
$L_y = 3$ μm, $\epsilon_r = 2$	1.9838	2.0466
$L_y = 6$ μm, $\epsilon_r = 2$	1.5096	1.5143

sponding to a heavily scattering analyzer), any change in certain incident field modes will pass through with hardly any such averaging at all. As a result of this diminished set of open channels, spatial sensitivity is enhanced.

We have shown that intensity correlation information of object position is enhanced with use of the analyzer. This means that, in a given noisy environment, we should be able to reach deeper into subwavelength geometrical features of objects under investigation. However, the efficacy in doing so will relate to experimental specifics. A heavily scattering analyzer will only be sensitive to changes in its open eigenchannels. In our experimental and numerical results so far [1], the changes being sensed have all continued to excite this shrinking subset of open eigenchannels. However, it also suggests the possibility of engineering the transmission matrix of an analyzer to be sensitive to changes in only a desired subset of field modes.

VI. DISCUSSION

Our interest has been the character of a randomly scattering analyzer placed in front of a detector array. This provides a new perspective to earlier work, where it was found that intensity correlations over translated incident field position allow retrieval of the field incident on a random medium based on transmission speckle intensity data as a function of translated field position [33]. Now we understand that the randomly scattering medium can be adapted to achieve increased spatial sensitivity to subwavelength geometrical features of an object in the far-field with motion in structured illumination. Likewise, the idea of coherent imaging in a heavily scattering random medium [8] can be re-interpreted in terms of the intervening random scatter (such as due to tissue) acting as an analyzer.

Discrepancies are found in Fig. 2 between the empirical eigenvalue distributions (T_n) and the theoretical bimodal distribution. The peak near $T = 0$ is prominent, though the one near $T = 1$ is not, despite evidence for both in Table II. As shown in Fig. 5, the discrepancy is understood as a consequence of the non-uniformity of x_n, which are related to T_n by (8). This uniformity is a necessary condition for the bimodal distribution to hold, as is detailed in Appendix B. Nonetheless, the increasing proportion of closed channels with more scatter in the analyzer is an important conclusion that is consistent with earlier studies of the bimodal density function where most eigenchannels are either fully "closed" or fully "open" [2, 13, 34, 35]. Importantly, there is evidence that regulating the scattering properties of the analyzer influences the achievable sensing resolution.

The quarter-circle distribution shows close agreement with the singular value distributions of $\Re(\mathbf{T})$ and $\Im(\mathbf{T})$, despite their lack of both symmetry and independently distributed matrix entries. This greater degree of agreement with the quarter-circle distribution than with the bimodal distribution (of the singular values σ and eigenvalues T_n, respectively) is notable, and may indicate differing rates of convergence to these two distributions.

Following the discussion of subwavelength far-field sensitivity in Sect. V, a question naturally arises regarding the limit of such a technique. One relevant concern applies to both sensitivity and imaging: uniqueness of the data. If two inputs (positions of an object, for example) happen to yield identical sets of measurements, then neither distinguishability nor inversion for such inputs is possible. If uniqueness can be assumed for at least a subset of possible inputs though, then inversion (and therefore imaging) can always be done, in theory, though the computational efficiency of such a practice is often reliant upon further assumptions. A second fundamental concern is the accuracy and precision of the measurements involved. These relate to the signal-to-noise ratio (SNR) of the measurements and number of bits used by the sensor's analog-to-digital converter (ADC). The law of large numbers [29] states that, if enough independent and identically distributed samples can be drawn from a distribution, then the sample mean can be made arbitrarily close to the true mean, effectively achieving an arbitrarily high SNR. In this context, this means that, with sufficient sampling, any arbitrarily small difference in datasets can be distinguished. One mitigation on this somewhat idealistic outlook is that, in practice, most sources of noise are not time-invariant, meaning that an arbitrarily high number of independent measurements is impossible to achieve (this is also true for other practical reasons, such as patience). A second, more subtle complication is that of sampling. For computational methods such as the one discussed here, comparisons can only be made between the discretized versions of data output by the ADC. If the difference between inputs is small enough, then the corresponding datasets may differ by an amount smaller than this discretization, bringing back the uniqueness issue and making these datasets indistinguishable no matter how much averaging one does. To be clear, these limiting issues of accuracy and precision exist in all cases where digital processing is performed on experimentally derived data, regardless of whether a scattering analyzer is used, and our method does not purport to bypass them; it merely approaches them more quickly than if a scattering analyzer were not used.

Various subsequent steps could be interesting. This work raises the prospect of regulating the statistical properties of a random medium to achieve high spatial sensitivity to changes in the incident field. For instance, aperiodic structures have field-control properties that are dependent on the specific geometrical features of the structure [36]. We now find a relationship between structures that may be designed for a specific task and the general statistical character of a random medium acting as an analyzer for super-resolution spatial sensing. The analyzer is acting in a compressed sensing framework [37], where, in our case, spatial field information is encoded in speckle from multiply scattered light. Optical scatter

is already being employed in the field of lensless imaging, in which the traditional lens is replaced with a thin diffuser. 3D imaging is enabled using a convolutional forward model [38], and while increasing the amount of scatter would likely invalidate such an approach, it could result in higher spatial resolution. One-way functions (functions that are computationally easy to compute but difficult to invert) form the basis of modern cryptography, but replacements are increasingly being sought for existing methods such as prime factorization and discrete logarithms [39]. Physical one-way functions have been studied as a potential alternative, and their effectiveness is hinged upon the sensitivity of a heavily scattering medium [40]. Designing a scattering analyzer using an asymmetric-transfer-function metasurface [41] could result in increased sensitivity compared to a random analyzer. Optimizing the spatial profile of the incident field has been shown to improve precision in estimations of parameters through diffuse media [42]. Such optimizations of the incident field could be combined with the analyzer concept discussed here, possibly resulting in further improvements of estimation performance or greater sensitivity. All results have assumed monochromatic light. In an experiment, this implies suitably high coherence, and in the sense of speckle statistics, the light source requirements depend on the degree of scatter. It would be interesting to consider reduced coherence requirements in relation to enhanced spatial resolution with a random analyzer. With a thin analyzer, it may also be possible to utilize the axial wavelength separation resulting from the chromato-axial memory effect [43, 44] (dilation of the speckle pattern due to spectral shift) to separate wavelengths and draw upon enhanced spatial resolution (where "memory" indicates the approximate angular tracing of light transmitted through a thin scattering medium with incident beam angle). Finally, estimation of the axial separation of two incoherent point sources using a mode sorter [45] might be re-imagined in the context of a random analyzer.

VII. CONCLUSION

This work has developed the underlying theory of randomly scattering analyzers, built further understanding of random matrix theory and the physics of coherent transport, demonstrated a far-field super-resolution sensing capability, and offered a new dimension for metrology and other application domains. This remote sensing approach with a randomly scattering analyzer is applicable to all wave types for which a heavily scattering medium exists, and that are coherent enough to produce an effect analogous to optical speckle, and hence offers substantial scope for impact on the physical sciences. The presented random analyzer concept offers opportunities for sensing and microscopy where far-subwavelength spatial information is important. While we have treated the informational aspects of the analyzer, achieving identification is possible with calibration, as in the concept of motion in structured illumination [9]. Based upon the results presented, it may be possible that measured intensity data through a random analyzer can be inverted to form a super-resolution image.

Regarding random matrix theory, we have established that the eigenvalue distribution for the transmission matrix that represents a scattering analyzer provides an explanation for why a more heavily scattering analyzer results in faster speckle intensity decorrelation. We have compared the applicability of two different probability distributions to the empirical eigenvalue distributions obtained from our numerical simulations. When compared to appropriate datasets, our results show good agreement with the quarter-circle distribution, though the amount of scatter was likely insufficient for the upper peak of the bimodal distribution to appear.

VIII. ACKNOWLEDGMENT

This work was supported by the National Science Foundation (NSF) under grants 1618908 and 1909660, and by the Air Force Office of Scientific Research under grant FA9550-19-1-0067.

We would like to thank the two anonymous referees who reviewed our manuscript, whose insightful comments are much appreciated.

Appendix A: Simulation Details

Here we elaborate upon the different aspects of the numerical FEM [46] simulations that were used to calculate empirical eigenvalue and singular value probability distributions (Sect. III) involving the transmission matrix $\mathbf{T}$, as well as the simulations involving the apertures (Sect. V).

1. Mesh Generation

The accuracy of any FEM simulation depends heavily on the size of the mesh elements. The mesh must be fine enough that numerical errors are negligible, but increasing the element density beyond this point merely increases the computational burden without improving results. The mesh density was primarily controlled by reducing the maximum mesh element size, while allowing the elements to be smaller than this by a factor of 10 as necessary (determined automatically by the FEM software [46]). The resolution of "narrow regions" (also determined automatically) was further increased by a factor of 10.

During our tests for numerical convergence, we found that regions near rapid material variations need to be more finely meshed. Therefore, in order to achieve numerical convergence while minimizing the computational

resources required, the maximum mesh element size was changed for different parts of the geometry domain. The necessary mesh densities were found to differ for the eigenvalue simulations of Sect. III and the aperture simulations of Sect. V. For the eigenvalue simulations, subdomain 1 consists of all the 200-nm dielectric squares, and was meshed with a maximum element size of $\lambda/40$. Subdomain 2 consists of all the free space in the domain, and was meshed with a maximum element size of $\lambda/20$. Subdomain 3 consists of the two perfectly matched layers (PMLs), and was also meshed with a maximum element size of $\lambda/20$.

When meshing the apertures for Sect. V, care was taken to ensure that the mesh density near the apertures was high enough. The region near the aperture(s), both inside and outside the film, was meshed to a maximum element size of $\lambda/80$, while the rest of the free space had a maximum element size of only $\lambda/50$. The dielectric squares were meshed with a maximum element size of $\lambda/100$. The maximum element size of the PMLs was increased to $\lambda/10$.

We also found that the square corners of the thick PEC film (but not the corners of the dielectric scatterers) had a slight singularity effect, so they were rounded to a radius of 1 nm to mitigate this effect.

2. Scatterers

The specified breadth and thickness of the scattering analyzer define its volume, which was discretized into 200-nm square regions. Exactly 50% of these were filled with dielectric material, with the rest being free space. The locations of the dielectric squares were randomized, with the distribution of all possible sets of dielectric positions being a uniform one.

It should be noted that the scattering properties of the simulated version of the analyzer are different from those of the analyzer used in previous experiments [1]. First, the TiO_2 scatterers in the experiments were 50 nm across, making them smaller than the simulated ones. Also, the scatterers in the experiment were far apart compared to the wavelength, whereas that property does not hold in the simulation. The reason for these changes is that we are able to achieve an increased level of scatter in a smaller simulation domain, which reduces the computational burden to a manageable level.

3. Boundary Conditions

To the left and right of the scattering analyzer (the x-axis boundaries) were Floquet periodic boundary conditions, The associated Floquet wave vector had discrete $k_x = 2\pi/L_x$, consistent with the discrete plane wave spectrum. Note that, because of this equality, this Floquet boundary condition is equivalent to a continuity boundary condition, as the phase progression between boundaries becomes zero.

Above and below the scattering analyzer (the y-axis boundaries) were free space regions. These were followed by PMLs, each with a thickness of 2λ, which are intended to minimize reflections in the scattered field formulation used, thereby simulating an infinite medium in the y dimension.

To implement the apertures in the PEC for Sect. V, the three rectangular shapes shown in green in Fig. 7 were first defined. The large rectangles left and right of the aperture construction were assigned each to have edges of infinitesimally thin PEC (except the ones that touch the periodic boundaries), and the insides of these rectangles were left as free space. For the two-aperture setup, the small central rectangular region was also given PEC edges. For the one-aperture setup, it was left as free space.

When the field magnitude was plotted just after the aperture system (at a distance of $\lambda/100$ away), it resulted in one or two spatial pulses of approximately the same width as the one or two apertures (with centers coinciding appropriately), which is expected. The singularity effects mentioned in Appendix A 1 were minimal.

4. Field Generation

The incident plane wave was specified in the FEM software as a background field (electric polarized in the z direction, which was orthogonal to the 2D simulation plane), and the scattered field was solved for. The total field is then the sum of the background and scattered fields.

The spectrum of plane waves used for the transmission matrix simulations (Sect. III) was chosen to be the full set of propagating modes that are periodic in the geometry. Each such mode has a transverse wavenumber of $k_x = mk_{x0}$, where $k_{x0} = 2\pi/L_x$ and the integer m spans the range $-m_{\max} \le m \le m_{\max}$. The maximum mode $m_{\max}$ was chosen as the highest-order propagating plane wave that is periodic over the geometry, or

$$m_{\max} = \left\lfloor \frac{k_0}{k_{x0}} \right\rfloor = \left\lfloor \frac{2\pi/\lambda}{2\pi/L_x} \right\rfloor = \left\lfloor \frac{L_x}{\lambda} \right\rfloor .$$

In our case, with $L_x = 60$ μm and $\lambda = 850$ nm, we get $m_{\max} = 70$, for a total of $N = 2m_{\max} + 1 = 141$ plane-wave modes. The two outermost plane waves (for which $m = \pm m_{\max}$) have angles of ± 1.4416 radians.

For the aperture simulations (Sect. V), only the $m = 0$ mode was used for the incident field, which corresponds to the plane wave perpendicular to the scattering analyzer. These field passed through the aperture system (which consisted of either one or two apertures, as shown in Fig. 7), thereby generating the discrete plane wave spectrum.

5. Detection and Processing

The detector plane was located a distance of 4λ away from the scattering analyzer, along which all the detector points are located. The detector plane spanned the entire breadth of the geometry.

Our goal is to measure only the far field and minimize the effect of evanescent fields, but the choice of detector plane distance is not trivial. Because the periodic boundary conditions make the scattering analyzer infinite in breadth, it becomes impossible to use a heuristic for the far-field distance based on analyzer size. If we instead model the analyzer as a collection of small apertures of size equal to the 200-nm dielectric squares, then the far-field distance becomes approximately $2(\lambda/4)^2/\lambda = \lambda/8$ (since $\lambda = 850$ nm). The chosen 4λ distance was settled on by gradually increasing the distance until the field statistics (as listed in final column of Table I) appeared to converge. Specifically, the Medium Scatter slab was chosen for this convergence analysis and showed a change in mean CR of about 0.5% between detector distances of 4λ and 5λ. The other analyzer configurations also showed mean CRs closer to 1 at 4λ than at 1λ, meaning that the statistics became closer to zero-mean circular Gaussian. Another near-field effect of note is optical vortices [47, 48], which involve small regions of alternating positive and negative time-average Poynting vector (in our case, the component normal to the detector plane). These were noticed in our simulations, but their effect had significantly decayed by the chosen distance of 4λ.

For the transmission matrix simulations, N detectors were uniformly distributed along the detector plane, and they detected the z component of the total electric field (background plus scattered). Because of the periodic boundary conditions on either side, it would be redundant to have detectors on both endpoints of the detector plane (as they would detect the same value). In order to gain true periodicity, we therefore instead calculated $N + 1$ uniformly distributed points along the detector plane and place detectors on N of these, omitting one of the endpoints. These N values were then passed through a discrete Fourier transform in order to calculate the entries of the matrix $\mathbf{T}$, which we have thereby ensured is a square matrix (as is assumed in Sect. II).

For the aperture simulations, periodicity is not a concern because we are not calculating a transmission matrix, so we are free to use more than N detectors. In this case, we uniformly distributed detectors along the detection plane with a separation interval of $\lambda/100$. These were configured to detect the y component of the Poynting vector of the total field (again, background plus scattered).

The aperture system was shifted in intervals of $\lambda/10$ parallel to the x axis, up to maximum distances of $\lambda/2$ in each direction. For each position of the aperture system, the speckle intensity pattern was measured at the detector plane. These speckle patterns were pairwise correlated using the Pearson correlation coefficient, and these coefficients were averaged together to form Fig. 8. Let s_y be the shift distance of the aperture system, so that $s_y = m \cdot (\lambda/10)$ for $m \in \{-5, -4, \ldots, 5\}$. Also, let $1 \le n \le N$ refer to the $(N = 10)$ different instances of the random analyzer. Therefore, if $C_P(s_{y1}, s_{y2}, n)$ is the Pearson correlation coefficient between aperture positions s_{y1} and s_{y2} for the nth random analyzer, then the average Pearson correlation coefficient for relative distance Δs_y is

$$C(\Delta s_y) = \frac{1}{N}\frac{1}{|S(s_y)|}\sum_{n=1}^{N}\sum_{\{s_{y1},s_{y2}\in S(s_y)\}} C_P\left(s_{y1}, s_{y2}, n\right), \tag{A1}$$

where $S(s_y)$ is the set of all shift distances s_{y1},s_{y2} such that $s_y = |s_{y1} - s_{y2}|$.

Appendix B: Derivation of Random Medium Transfer Matrix and Bimodal Density Function

The derivation of the bimodal probability density function is developed here for completeness, and because we are unaware of this having been done elsewhere. It begins with consideration of the matrices that the eigenvalues belong to.

During the mid-to-late 1980s, motivated in part to develop quantum transport theory in disordered systems and build on the work of Landauer and others [49], a multitude of papers considered various mathematical aspects, as summarized in Beenakker's review paper [2]. We draw on specific parts of this body of work only to provide background for our treatment of random matrix theory for the analyzer problem.

1. Symplectic Character of Transfer Matrix

The electromagnetic scattering matrix, relating the incident to scattered wave amplitudes through four sub-matrices, is reciprocal (with time-reversal symmetry) and unitary (lossless materials), resulting in

$$\mathbf{S}\mathbf{S}^H = \mathbf{I}, \tag{B1}$$

with

$$\mathbf{S} = \begin{bmatrix} \mathbf{S}_{11} & \mathbf{S}_{21} \\ \mathbf{S}_{12} & \mathbf{S}_{22} \end{bmatrix} = \begin{bmatrix} \mathbf{R} & \mathbf{T}' \\ \mathbf{T} & \mathbf{R}' \end{bmatrix}, \tag{B2}$$

where the subscript notation on the scattering parameters is broadly used in some literature, and lower-case variants of the reflection and transmission sub-matrices is common in the quantum transport literature drawn upon here [2]. In general, the four $N \times N$ sub-matrices of $\mathbf{S}$ represent non-symmetry (differing $\mathbf{S}_{11}$ and $\mathbf{S}_{22}$) and non-reciprocity (differing $\mathbf{S}_{21}$ and $\mathbf{S}_{12}$). With a lossless reciprocal system, we have $\mathbf{S}^H = \mathbf{S}^{-1}$. Additionally, time-reversal invariance gives $\mathbf{S} = \mathbf{S}^\top$, where $^\top$ denotes the

(non-conjugate) transpose [2, 16]. We utilize the transmission matrix, $\mathbf{T}$ in our work here, and $\mathbf{S}_{21} = \mathbf{S}_{12} = \mathbf{T}$ because of this symmetry [50, 51], and because the wave impedances are identical on either side of the random analyzer. Using the notation of Beenakker [2], we have

$$\mathbf{c}^{\text{out}} = \mathbf{S}\mathbf{c}^{\text{in}}, \tag{B3}$$

with $\mathbf{c}^{\text{in}}$ the vector of complex incident mode coefficients (multiple modes incident from, say, two ports: the left and the right) and $\mathbf{c}^{\text{out}}$ that for the scattered amplitudes (at the two ports). It is useful to explicitly split $\mathbf{c}^{\text{in}}$ into $\mathbf{a}_l$ and $\mathbf{b}_r$ (incoming on the left and right ports, respectively), and split $\mathbf{c}^{\text{out}}$ into $\mathbf{b}_l$ and $\mathbf{a}_r$ (outgoing on the right and left ports, respectively), a notation used by Imry [14] and by Pichard and André [15] (see either of these references for a diagram). This version of (B3) yields

$$\begin{bmatrix} \mathbf{b}_l \\ \mathbf{a}_r \end{bmatrix} = \mathbf{S} \begin{bmatrix} \mathbf{a}_l \\ \mathbf{b}_r \end{bmatrix}. \tag{B4}$$

Using a standard transformation, one can write the useful transfer matrix, which relates output (port 2) quantities to those at the input (port 1) as

$$\mathbf{c}^{\text{right}} = \mathbf{M}\mathbf{c}^{\text{left}} \tag{B5}$$

$$\begin{bmatrix} \mathbf{a}_r \\ \mathbf{b}_r \end{bmatrix} = \mathbf{M} \begin{bmatrix} \mathbf{a}_l \\ \mathbf{b}_l \end{bmatrix}, \tag{B6}$$

where $\mathbf{M}$ is $2N \times 2N$ and written as

$$\mathbf{M} = \begin{bmatrix} \mathbf{A} & \mathbf{B} \\ \mathbf{C} & \mathbf{D} \end{bmatrix}. \tag{B7}$$

Here we use an upper case Roman notation, rather than the lower-case Greek equivalents in Mello, Pereyra, and Kumar [16]. The transfer matrix is useful for cascading systems, because the overall transfer matrix becomes simply a product of each sub-system transfer matrix. The eigenvalues of $\mathbf{M}^H\mathbf{M}$ are real because the matrix product is real and symmetric.

In quantum transport, conservation of current flux is considered, but in our work, it is conservation of power (through the Poynting vector, or energy per unit time) that is imposed. However, this is a mathematical detail. Conservation conditions lead to [52]

$$\mathbf{M}^H\mathbf{\Sigma}\mathbf{M} = \mathbf{\Sigma}, \tag{B8}$$

where

$$\mathbf{\Sigma} = \begin{bmatrix} \mathbf{I} & \mathbf{0} \\ \mathbf{0} & -\mathbf{I} \end{bmatrix}, \tag{B9}$$

with $\mathbf{I}$ and $\mathbf{0}$ being the $N \times N$ identity and zero matrices, respectively. As a result of this symplectic property (which has also been referred as "pseudo-unitarity" [2]), Pichard and Sarma [53] noted that real transfer matrices are symplectic, as are products. From time-reversal invariance [54],

$$\mathbf{M} = \begin{bmatrix} \mathbf{A} & \mathbf{B} \\ \mathbf{B}^* & \mathbf{A}^* \end{bmatrix}, \tag{B10}$$

where * denotes the element-wise complex conjugate. As a result of flux (power) conservation and time-reversal invariance, the elements of the transfer matrix satisfy [16]

$$\mathbf{A}^H\mathbf{A} - \mathbf{B}^\top\mathbf{B}^* = \mathbf{I} \tag{B11}$$

$$\mathbf{A}^H\mathbf{B} = \mathbf{B}^\top\mathbf{A}^*. \tag{B12}$$

In noting from (B8) that $|\det(\mathbf{M})| = 1$, that $\det(\mathbf{M})$ is real, and (based on analytic continuity) that $\det(\mathbf{M}) = 1$, it can be shown that $\mathbf{M}$ is symplectic under the more typically used definition, involving a skew-symmetric matrix, rather than one such as $\mathbf{\Sigma}$ with structure given in (B9). The symplectic nature of $\mathbf{M}$ is proven ([16], Appendix A) by decomposing $\mathbf{M}$ into real sub-matrices to yield $\mathbf{M}^\top\mathbf{\Omega}\mathbf{M} = \mathbf{\Omega}$, when combined with (B11) and (B12). This yields the standard symplectic form, with $\mathbf{\Omega}$ skew symmetric ($2N \times 2N$) and $\mathbf{\Omega}^\top\mathbf{\Omega} = \mathbf{I}$.

The pseudo-unitary character of $\mathbf{M}$ allows us to write, from (B8),

$$\mathbf{M}^H = \mathbf{\Sigma}\mathbf{M}^{-1}\mathbf{\Sigma} \tag{B13}$$

$$\mathbf{M}^{-1} = \mathbf{\Sigma}\mathbf{M}^H\mathbf{\Sigma}, \tag{B14}$$

since $\mathbf{\Sigma}^{-1} = \mathbf{\Sigma}$. Consequently,

$$\begin{aligned} \left(\mathbf{M}^H\mathbf{M}\right)^{-1} &= \mathbf{M}^{-1}\left(\mathbf{M}^H\right)^{-1} \\ &= \left(\mathbf{\Sigma}\mathbf{M}^H\mathbf{\Sigma}\right)\left(\mathbf{\Sigma}\mathbf{M}^{-1}\mathbf{\Sigma}\right)^{-1} \\ &= \left(\mathbf{\Sigma}\mathbf{M}^H\mathbf{\Sigma}\right)\left(\mathbf{\Sigma}^{-1}\mathbf{M}\mathbf{\Sigma}^{-1}\right) \\ &= \mathbf{\Sigma}\mathbf{M}^H\mathbf{M}\mathbf{\Sigma}^{-1} \\ &= \mathbf{\Sigma}\mathbf{M}^H\mathbf{M}\mathbf{\Sigma} \qquad \text{(B15)} \\ &= \mathbf{\Sigma}^{-1}\mathbf{M}^H\mathbf{M}\mathbf{\Sigma}. \qquad \text{(B16)} \end{aligned}$$

This similarity transform result (B16) implies that the eigenvalues of $\left(\mathbf{M}^H\mathbf{M}\right)^{-1}$ must be identical to those of $\mathbf{M}^H\mathbf{M}$ [55]. In addition, because $\mathbf{M}$ and $\mathbf{M}^H$ are both symplectic, $\mathbf{M}^H\mathbf{M}$ will also be symplectic (demonstrated by (B15), due to conjugate symmetry of $\mathbf{M}^H\mathbf{M}$), and will have real and positive eigenvalues that occur in inverse pairs [14, 56].

2. Relating the Scattering and Transfer Matrices

From here until (B35), we follow a line from Pichard's 1984 PhD thesis [57]. This derivation is also reviewed in part by Imry [14]. Applying (B14) with (B7) and (B9) yields

$$\mathbf{M}^{-1} = \begin{bmatrix} \mathbf{A}^H & -\mathbf{C}^H \\ -\mathbf{B}^H & \mathbf{D}^H \end{bmatrix}. \tag{B17}$$

From $\mathbf{M}^{-1}\mathbf{M} = \mathbf{I}$, one finds

$$\mathbf{A}^H\mathbf{A} - \mathbf{C}^H\mathbf{C} = \mathbf{I} \tag{B18}$$

$$\mathbf{A}^H\mathbf{B} - \mathbf{C}^H\mathbf{D} = \mathbf{0} \tag{B19}$$

$$-\mathbf{B}^H\mathbf{A} + \mathbf{D}^H\mathbf{C} = \mathbf{0} \tag{B20}$$

$$-\mathbf{B}^H\mathbf{B} + \mathbf{D}^H\mathbf{D} = \mathbf{I}. \tag{B21}$$

Using (B7), (B15), (B18), and (B21), it is found that

$$\begin{aligned}\mathbf{M}^H\mathbf{M} + \left(\mathbf{M}^H\mathbf{M}\right)^{-1} &= 2\begin{bmatrix}\mathbf{A}^H\mathbf{A} + \mathbf{C}^H\mathbf{C} & \mathbf{0} \\ \mathbf{0} & \mathbf{B}^H\mathbf{B} + \mathbf{D}^H\mathbf{D}\end{bmatrix} \\ &= 2\begin{bmatrix}2\mathbf{A}^H\mathbf{A} - \mathbf{I} & \mathbf{0} \\ \mathbf{0} & 2\mathbf{D}^H\mathbf{D} - \mathbf{I}\end{bmatrix}. \end{aligned} \tag{B22}$$

Here, Pichard lists out the full set of equations specified by the matrices $\mathbf{S}$, $\mathbf{M}$, and $\mathbf{M}^{-1}$, using (B4), (B6), and (B17):

$$\mathbf{a}_r = \mathbf{A}\mathbf{a}_l + \mathbf{B}\mathbf{b}_l \tag{B23}$$
$$\mathbf{b}_r = \mathbf{C}\mathbf{a}_l + \mathbf{D}\mathbf{b}_l \tag{B24}$$
$$\mathbf{a}_l = \mathbf{A}^H\mathbf{a}_r - \mathbf{C}^H\mathbf{b}_r \tag{B25}$$
$$\mathbf{b}_l = -\mathbf{B}^H\mathbf{a}_r + \mathbf{D}^H\mathbf{b}_r \tag{B26}$$
$$\mathbf{a}_r = \mathbf{T}\mathbf{a}_l + \mathbf{R}'\mathbf{b}_r \tag{B27}$$
$$\mathbf{b}_l = \mathbf{R}\mathbf{a}_l + \mathbf{T}'\mathbf{b}_l. \tag{B28}$$

Using these, a set of relationships is deduced between the elements of $\mathbf{S}$ and those of $\mathbf{M}$,

$$\mathbf{R} = -\mathbf{D}^{-1}\mathbf{C} \tag{B29}$$
$$\mathbf{T}' = \mathbf{D}^{-1} \tag{B30}$$
$$\mathbf{T} = \left(\mathbf{A}^H\right)^{-1} \tag{B31}$$
$$\mathbf{R}' = \left(\mathbf{A}^H\right)^{-1}\mathbf{C}^H. \tag{B32}$$

It can be shown that these satisfy (B23) through (B28).

Using (B29) through (B32), (B22) becomes

$$\begin{aligned}\frac{1}{4}\mathbf{M}^H\mathbf{M} + \left(\mathbf{M}^H\mathbf{M}\right)^{-1} + \frac{1}{2}\mathbf{I} \\ = 2\begin{bmatrix}\left(\mathbf{T}^H\mathbf{T}\right)^{-1} & \mathbf{0} \\ \mathbf{0} & \left(\mathbf{T}'\mathbf{T}'^H\right)^{-1}\end{bmatrix},\end{aligned} \tag{B33}$$

where $\mathbf{I}$ is now the $2N \times 2N$ identity matrix, rather than $N \times N$. Inverting gives

$$\begin{aligned}\left[\mathbf{M}^H\mathbf{M} + \left(\mathbf{M}^H\mathbf{M}\right)^{-1} + 2\mathbf{I}\right]^{-1} &= \frac{1}{4}\begin{bmatrix}\mathbf{T}^H\mathbf{T} & \mathbf{0} \\ \mathbf{0} & \mathbf{T}'\mathbf{T}'^H\end{bmatrix} \\ &= \frac{1}{4}\begin{bmatrix}\mathbf{T}^H\mathbf{T} & \mathbf{0} \\ \mathbf{0} & \mathbf{T}\mathbf{T}^H\end{bmatrix},\end{aligned} \tag{B34}$$

because $\mathbf{T} = \mathbf{T}'$. Taking the trace (Tr) gives

$$\mathrm{Tr}\left(\mathbf{T}^H\mathbf{T}\right) = 2\mathrm{Tr}\left\{\left[\mathbf{M}^H\mathbf{M} + \left(\mathbf{M}^H\mathbf{M}\right)^{-1} + 2\mathbf{I}\right]^{-1}\right\}. \tag{B35}$$

It should be noted that this result is exact, and not an approximation [14, 15, 57].

3. Transmission Eigenvalues and Conductance

We adapt a theory that was developed for electron transport and localization [50] and under the assumption of low conductance leads to the approximation that the conductance g is given by $\mathrm{Tr}\left(\mathbf{T}^H\mathbf{T}\right)$ (in units of e^2/h, with a factor of two to account for spin). Work in the early 1980s to generalize from one such transmission channel [58] to many channels argued that, since the overall conductance was finite, the transmission probability of each individual channel must be small [50, 51, 59]. Perhaps most notably, it has also been derived using an assumption that the conductor length is much greater than the mean free path length [60, 61]. This interpretation draws a direct analogy between the transport of electrons through a long disordered region and of photons through a thick scattering region.

In our case of the field transmission matrix, we can consider this conductance relationship as being exact [4]. We can thus write

$$g = \mathrm{Tr}\left(\mathbf{T}^H\mathbf{T}\right) = \sum_{n=1}^{N} T_n, \tag{B36}$$

where the T_n are the eigenvalues of $\mathbf{T}^H\mathbf{T}$, without approximation as $N \to \infty$. Using (B36), the mean conductances of each of the types of randomly scattering analyzer are calculated, and the results are shown in Table V. Here, the normalization discussed in Sect. IV A was applied, not because a direct comparison to a probability distribution for g is being made, but in order to account for the incident power used when calculating T_n. Notice that these conductance values decrease as the amount of scatter in the analyzer increases, while the number of eigenchannels remains constant ($N = 141$). This indicates that the transmission eigenvalues (T_n) themselves are becoming smaller, behavior that is analogous to the low-transmission approximation from electron transport theory that leads to its version of (B36). This suggests that we are getting closer to the limit in which the bimodal distribution applies as the level of scatter increases, though we may not have reached this regime with these slab types.

4. Transmission Matrix and Transfer Matrix Eigenvalues

Mello and Pichard [62] prove that $\mathbf{M}$ can be decomposed in an orthogonal basis as

$$\mathbf{M} = \mathbf{U}\begin{bmatrix}\sqrt{\mathbf{I} + \boldsymbol{\lambda}} & \sqrt{\boldsymbol{\lambda}} \\ \sqrt{\boldsymbol{\lambda}} & \sqrt{\mathbf{I} + \boldsymbol{\lambda}}\end{bmatrix}\mathbf{V}, \tag{B37}$$

with $\mathbf{U}$ and $\mathbf{V}$ unitary, and $\boldsymbol{\lambda}$ a diagonal, real, positive matrix. This form was presented in earlier work [16, 63].

It has been stated that [14, 15, 56] (for a proof, see

TABLE V. The mean conductance, calculated using (B36), for the five types of randomly scattering analyzer that are listed in Table I. The same normalization was performed for this calculation as has been used elsewhere (see Sect. IV A). The conductance g was calculated for each instance of the randomly scattering analyzers, and these conductances were averaged together for each type.

Slab Type	Mean Conductance g
Lowest Scatter	37.357
Low Scatter	28.037
Medium Scatter	24.426
High Scatter	15.669
Highest Scatter	11.605

Ref. [64])

$$\mathbf{X} = \frac{1}{4}\left[\mathbf{M}^H\mathbf{M} + \left(\mathbf{M}^H\mathbf{M}\right)^{-1} - 2\mathbf{I}\right] \tag{B38}$$

$$= \mathbf{V}^H \begin{bmatrix} \boldsymbol{\lambda} & \mathbf{0} \\ \mathbf{0} & \boldsymbol{\lambda} \end{bmatrix} \mathbf{V}, \tag{B39}$$

where $\mathbf{X}$ is defined to have this form and the diagonalization was shown to result. This indicates that $\boldsymbol{\lambda}$ in (B39) contains the unique eigenvalues of $\mathbf{X}$. It has been shown [64] and indicated [14–16, 56] that (B39) leads to

$$\mathrm{Tr}\left(\mathbf{T}^H\mathbf{T}\right) = \sum_{n=1}^{N} \frac{1}{1+\lambda_n}, \tag{B40}$$

where λ_n are the eigenvalues of the $2N \times 2N$ matrix $\mathbf{X}$ in (B38), and the λ_n constitute the diagonal entries in the $\boldsymbol{\lambda}$ matrices in (B37) and (B39). Comparing (B40) with the second relationship in (B36), we have

$$T_n = \frac{1}{1+\lambda_n}. \tag{B41}$$

The eigenvalues Λ_n of $\mathbf{M}^H\mathbf{M}$ come in inverse pairs, because of the symplectic character of $\mathbf{M}$ [14]. With a view to a Lyapunov exponent form [65], we can thus assign $\exp(\pm 2x_n)$ to these eigenvalues. Using this perspective motivates a mapping

$$\frac{1}{1+\lambda_n} = \frac{2}{1+\cosh 2x_n}, \tag{B42}$$

so that

$$\lambda_n = \cosh^2 x_n - 1. \tag{B43}$$

As a result, and from (B41),

$$T_n = \frac{1}{\cosh^2 x_n}, \tag{B44}$$

so the conductance can be written exactly in the limit as [2, 21]

$$g = \mathrm{Tr}\left(\mathbf{T}^H\mathbf{T}\right) = \sum_{n=1}^{N} \frac{1}{\cosh^2 x_n}. \tag{B45}$$

Again, these T_n are the eigenvalues of the matrix $\mathbf{T}^H\mathbf{T}$, which in this work are plotted in Fig. 2. Under conditions where x_n is uniformly distributed, we will prove that T_n has a bimodal density function.

5. Uniform Distribution for x_n

The asymptotic Lyapunov behavior is established from the large length limit, and this can be represented as the multiplication of $\mathbf{M}_i$, where this is the transfer matrix for the ith thin scattering layer. The multiplicative character of $\mathbf{M}$ has been presented a basis for x_n being uniformly distributed [65]. The situation where the x_n are uniformly distributed has been called the metallic diffusive regime [2] (see page 774). We review the basis of this representation, because it is used along with (B44) to prove bimodal character in the limit of sufficient random scatter.

Nieuwenhuizen and van Rossum [21] utilize (B44) and the assumption that the Lyapunov coefficients x_n are uniformly distributed to study the transmission character of multiply scattered waves and note that this is the case under very general conditions. Numerical evidence for the approximately uniform nature of x_n has been found [15]. Starting with the DMPK equation, Beenakker derives the uniform density result for the diffusive regime (see [2], page 764). Mello and Pichard [17] explain the resulting uniform density as a result of associating each eigenchannel of the disordered system with a localization length that characterizes its exponential decay in transmission. In the limit of many channels, this results in a uniform density function for x_n. They also note that the trend for the Lyapunov exponents to be uniform appears to be rather generic, noting the example of dynamic systems. In our work, we find that as the amount of scatter in the analyzer increases, we approach a uniform density for x_n based on numerical calculations for the random analyzer situation that we treat.

6. Bimodal Density Function

The final step in this derivation is to develop the probability density function for T_n, given in (B44), into the bimodal density function (Eq. (251) in [2]) that appears in (7). This is done by incorporating the assuming that x_n is uniformly distributed, using a simplified random variable notation.

The development here is based on material in Davenport and Root [66] (pages 33–35) and van Kampen [67] (pages 17–18). When notation differs between these two sources, we prefer that of van Kampen, where random variables are capitalized. Let X be a real-valued random variable that can take on values $X \in S_X$. Let $Y[X]$ be a real-valued function of X, making it also a random variable. This Y can be considered a mapping from the space S_X to a new space S_Y, where $Y \in S_Y$.

Assume that the probability density function for X exists, denote it as $p_X(x)$, and assume that it is continuous almost everywhere. It can be shown that, if the probability density function of Y exists (denoted $p_Y(y)$), Y is a differentiable monotonic function of X, and $\mathrm{d}Y/\mathrm{d}X$ vanishes only at isolated points, then a direct relation can be written between $p_X(x)$ and $p_Y(y)$. It can then be shown that, if $S_Y(y)$ is the interval $-\infty < Y \leq y$ (for some y), then there exists an $x(y)$ such that $S_X(y)$ is the interval $-\infty < X \leq x(y)$. The general relationship then becomes

$$p_Y(y) = p_X(x(y)) \left| \frac{\mathrm{d}x}{\mathrm{d}y} \right|, \tag{B46}$$

with $|\mathrm{d}x/\mathrm{d}y|$ the Jacobi determinant. We will use (B46) in the derivation of the bimodal density function.

Now consider the special case

$$Y = \frac{1}{\cosh^2 X}, \tag{B47}$$

or equivalently, with a one-to-one mapping,

$$X = \cosh^{-1}\left(\frac{1}{\sqrt{Y}}\right), \tag{B48}$$

and for $Y \geq 0$ and $X \geq 0$. Note that (B48) diverges as $Y \to 0$. Equations (B47) and (B48) satisfy the aforementioned requirements. Because Y cannot be negative,

$$\begin{aligned} &P(Y \leq y) = 0 \quad \text{for} \quad y < 0 \\ \implies &p_Y(y) = 0 \quad \text{for} \quad y < 0. \end{aligned} \tag{B49}$$

$S_X(y)$ is the set of points $0 \leq X \leq \cosh^{-1}\left(1/\sqrt{y}\right)$ for $y \geq 0$. Therefore,

$$\begin{aligned} P(Y \leq y) &= P\left[0 \leq X \leq \cosh^{-1}\left(\frac{1}{\sqrt{y}}\right)\right] \\ &= P\left[X \leq \cosh^{-1}\left(\frac{1}{\sqrt{y}}\right)\right] - P[X < 0] \\ &= P\left[X \leq \cosh^{-1}\left(\frac{1}{\sqrt{y}}\right)\right]. \end{aligned} \tag{B50}$$

Writing this probability in terms of $p_X(x)$, we have

$$P(Y \leq y) = \int_0^{\cosh^{-1}\left(\frac{1}{\sqrt{y}}\right)} p_X(x)\mathrm{d}x. \tag{B51}$$

Taking the derivative of (B51), and use of (B46), leads to

$$\begin{aligned} \frac{\mathrm{d}P(Y \leq y)}{\mathrm{d}y} &= p_Y(y) \\ &= p_X\left(x = \cosh^{-1}\frac{1}{\sqrt{y}}\right) \cdot \left|\frac{\mathrm{d}x}{\mathrm{d}y}\right|. \end{aligned} \tag{B52}$$

Now consider the special case of a uniform density function over a continuous interval. Let $S_X = [0, \hat{S}_X]$, giving

$$p_X(x) = \begin{cases} 1/\hat{S}_X & \text{if } x \in [0, \hat{S}_X] \\ 0 & \text{otherwise} \end{cases}. \tag{B53}$$

A point $X = x$ is related to $Y = y$ by

$$x = \cosh^{-1}\frac{1}{\sqrt{y}}. \tag{B54}$$

To obtain $p_Y(y)$, we form

$$\frac{\mathrm{d}x}{\mathrm{d}y} = \frac{\mathrm{d}}{\mathrm{d}y}\left(\cosh^{-1}\frac{1}{\sqrt{y}}\right). \tag{B55}$$

From Abramowitz and Stegun [68], page 88,

$$\frac{\mathrm{d}}{\mathrm{d}z}\left(\cosh^{-1} z\right) = \left(z^2 - 1\right)^{-1/2}. \tag{B56}$$

With $z = 1/\sqrt{y}$, $\mathrm{d}z/\mathrm{d}y = -y^{-3/2}/2$. We thus have, with use of the chain rule for differentiation,

$$\begin{aligned} \frac{\mathrm{d}}{\mathrm{d}y}\left(\cosh^{-1}\frac{1}{\sqrt{y}}\right) &= \frac{\mathrm{d}}{\mathrm{d}z}\left(\cosh^{-1} z\right) \cdot \frac{\mathrm{d}z}{\mathrm{d}y} \\ &= \left(\frac{1}{y} - 1\right)^{-1/2} \cdot \left(-\frac{1}{2}y^{-3/2}\right) \\ &= -\frac{1}{2}\frac{1}{y\sqrt{1-y}}. \end{aligned} \tag{B57}$$

With use of (B57) in (B46), we have

$$p_Y(y) = A_\delta \frac{1}{y\sqrt{1-y}}, \tag{B58}$$

where, in order to form a density function with a non-integrable singularity at $y = 0$, we have

$$A_\delta^{-1} = \int_\delta^\infty \frac{1}{y\sqrt{1-y}}\mathrm{d}y, \tag{B59}$$

with δ some small positive value. We have now arrived at the bimodal eigenvalue density function.

Appendix C: Quarter-Circle Distribution Background

This appendix gives a brief overview of the quarter-circle distribution, beginning with its origins in random-sign matrices and ending with a more general treatment that allows for complex-valued matrices. We end by discussing how the form of the quarter-circle distribution used in (10) relates to this line of work.

1. Random-Sign Matrices

The quarter-circle distribution originated during a derivation by Wigner of the eigenvalue distribution of random-sign real symmetric matrices [26]. It deals with real-valued symmetric matrices H of dimension $2N+1$, where N is very large. The diagonal elements are 0, and the non-diagonal elements $v_{ij} = v_{ji} = \pm v$ all have the same absolute value v but random signs. There are $2^{N(2N+1)}$ such matrices, and Wigner defines the kth moment as $M_k = \langle H^k \rangle_{00}$, where the brackets indicate averaging over all such matrices. Wigner calculates these moments M_k, and then uses these moments to calculate the probability density function (referred to in his work as the "strength function") $\sigma(x)$, where x represents the eigenvalues of H. This results in the quarter-circle distribution shown in Eq. (20a) of [26], which is

$$\sigma(x) = \frac{\sqrt{8Nv^2 - x^2}}{4\pi N v^2}, \tag{C1}$$

for $-v\sqrt{8N} < x < v\sqrt{8N}$.

The notation used throughout this appendix differs from that used in (10), instead having been chosen to agree with the literature that is being reviewed.

2. Gaussian Matrices

This set of constraints on these matrices was relaxed in a later work by Wigner [27], allowing the distribution to be applied to real symmetric Gaussian matrices. The revised requirements are then as follows.

- The matrix dimension is simply N, thereby allowing for matrices of either even or odd dimensionality.
- These matrices must still be real and symmetric, and there must be no statistical correlations between matrix elements, except for the condition of symmetry.
- Instead of requiring random-sign matrix elements, now the probability distributions of v_{ij} and v_{ji} just have to be the same.
- All of these probability distributions also must have an upper bound that is independent of i and j. This condition, when combined with the previous one, means that all the odd moments vanish to zero.
- The second moment of all v_{ij} must be the same, denoted by m^2.

Wigner notes that this last condition can be relaxed so that it holds for only a large majority for matrix elements, and that this relaxation allows use of the random-sign matrices considered in Ref. [26]. Using these conditions, Wigner arrives at the same quarter-circle distribution as in the earlier random-sign-matrix analysis. That eigenvalue distribution is

$$\sigma(x) = \frac{\sqrt{4Nm^2 - x^2}}{2\pi N m^2}, \tag{C2}$$

for $x^2 < 4Nm^2$. Note the similarity between (C1) and (C2) despite the different types of random matrices involved.

3. Complex Matrices

This line of work was further extended by Marčenko and Pastur [28] in several ways, notably allowing for complex-valued matrices. They begin by defining an operator $B_N(n)$ that acts in an N-dimensional unitary space H_N, which includes randomly distributed real random variables τ_i and complex vectors q_i (n of each), and is given by

$$B_N(n) = A_N + \sum_{i=1}^{n} \tau_i q^{(i)}(\cdot, q^{(i)}), \tag{C3}$$

where n is a nonrandom number, A_N is a nonrandom self-adjoint operator, and $(x, q^{(i)})$ is the scalar product in H_N between $q^{(i)}$ and some other vector x. They also denote $v(\lambda, B_N(n))$ as the probabilistic cumulative density function of the operator $B_N(n)$'s eigenvalues. They then consider the case $N \to \infty$, and assume that four conditions are satisfied.

- The limit $c = \lim_{N\to\infty}(n/N)$ exists.
- The sequence of normalized spectral functions for A_N converges as $N \to \infty$.
- The random vectors q_i have absolute moments to fourth order, and the even moments can be put into a form specified in Eqs. (1.4) through (1.6) of their paper [28].
- The random variables τ_i are independent and identically distributed.

The authors [28] go on to prove properties based on these assumptions. Then, as an example, they specify a certain $B_N(n)$ so that the operator becomes a projection onto the n-dimensional space spanned by the n complex random vectors q_i. Therefore, the corresponding cumulative distribution function $v(\lambda; B_N(n), c)$ becomes that of the eigenvalues for some complex random matrix, which is what we seek to calculate in this work. After showing that this form of $B_N(n)$ satisfies the four constraints listed above, they derive an expression for the cumulative density function $v(\lambda; B_N(n), c)$, as well as its first derivative with respect to λ, which is the corresponding probability density function. As $N \to \infty$, this eigenvalue density function converges to

$$\frac{dv(\lambda; B_N(n), c)}{d\lambda} = \frac{4c\tau^2 - \lambda^2}{2\pi c\tau^2}\left(1 + \frac{\lambda + \tau}{\tau c}\right)^{-1} \tag{C4}$$

for $\lambda^2 \leq 4c\tau^2$. The authors note that, in the limit $c \to \infty$, this becomes the same quarter-circle probability distribution that was arrived at by Wigner [26, 27]. This result is significant to us, because our random matrices are complex-valued.

4. In This Work

The quarter-circle density function that we use in (10), with $\sigma \in [0, 1]$ a random variable corresponding to the singular values of the appropriate random matrices (the real-valued $\Re(\mathbf{T})$ and $\Im(\mathbf{T})$), can be considered a simplified version (C2), where the distribution no longer has the range $[0, 4Nm^2)$ and explicit dependence on N and m has been dropped through the normalization procedure in Sect. IV A.

The required conditions for this distribution are met by independent and identically distributed Gaussian entries. Note that two Gaussian random variables being uncorrelated does not imply that they are independent, and that this independence is necessary for the quarter-circle distribution. Also, the matrices do not satisfy the symmetry requirement. An alternative approach would have been to use the Marčenko-Pastur law (which has different requirements) and compare it to $\sqrt{T_n}$, where T_n are the eigenvalues of $\mathbf{T}^H\mathbf{T}$.

[1] Q. Luo, J. A. Patel, and K. J. Webb, Phys. Rev. Res. **3**, L042045 (2021).
[2] C. W. J. Beenakker, Rev. Mod. Phys. **69**, 731 (1997).
[3] S. M. Popoff, G. Lerosey, R. Carminati, M. Fink, A. C. Boccara, and S. Gigan, Phys. Rev. Lett. **104**, 100601 (2010).
[4] Z. Shi and A. Z. Genack, Phys. Rev. Lett. **108**, 043901 (2012).
[5] S. M. Popoff, A. Goetschy, S. F. Liew, A. D. Stone, and H. Cao, Phys. Rev. Lett. **112**, 133903 (2014).
[6] I. M. Vellekoop and A. P. Mosk, Phys. Rev. Lett. **101**, 120601 (2008).
[7] P. Ambichl, W. Xiong, Y. Bromberg, B. Redding, H. Cao, and S. Rotter, Phys. Rev. X **7**, 041053 (2017).
[8] J. A. Newman, Q. Luo, and K. J. Webb, Phys. Rev. Lett. **116**, 073902 (2016).
[9] K. J. Webb, Y. Chen, and T. A. Smith, Phys. Rev. Appl. **6**, 024020 (2016).
[10] J. W. Goodman, *Statistical Optics* (John Wiley & Sons, 2015).
[11] I. S. Reed, IRE Trans. Inform. Theory **8**, 194 (1962).
[12] K. J. Webb and Q. Luo, Phys. Rev. A **101**, 063827 (2020).
[13] A. Goetschy and A. D. Stone, Phys. Rev. Lett. **111**, 063901 (2013).
[14] Y. Imry, EPL (Europhys. Lett.) **1**, 249 (1986).
[15] J. Pichard and G. André, EPL (Europhys. Lett.) **2**, 477 (1986).
[16] P. A. Mello, P. Pereyra, and N. Kumar, Ann. Phys. **181**, 290 (1988).
[17] P. A. Mello and J.-L. Pichard, Phys. Rev. B **40**, 5276 (1989).
[18] L. Mandel and E. Wolf, *Optical Coherence and Quantum Optics* (Cambridge University Press, 1995).
[19] J.-P. Berenger, J. Comput. Phys. **114**, 185 (1994).
[20] T. G. Mayerhöfer, S. Pahlow, and J. Popp, ChemPhysChem **21**, 2029 (2020).
[21] T. M. Nieuwenhuizen and M. C. W. van Rossum, Phys. Rev. Lett. **74**, 2674 (1995).
[22] O. Dorokhov, Solid State Commun. **51**, 381 (1984).
[23] J. Pendry, A. MacKinnon, and A. Pretre, Physica A **168**, 400 (1990).
[24] J. B. Pendry, A. MacKinnon, and P. J. Roberts, Proc. R. Soc. A **437**, 67 (1992).
[25] B. Gérardin, J. Laurent, A. Derode, C. Prada, and A. Aubry, Phys. Rev. Lett. **113**, 173901 (2014).
[26] E. P. Wigner, Ann. Math. **62**, 548 (1955).
[27] E. P. Wigner, Ann. Math. **67**, 325 (1958).
[28] V. A. Marčenko and L. A. Pastur, Mat. Sb. **1**, 457 (1967).
[29] A. Papoulis and S. U. Pillai, *Probability, Random Variables, and Stochastic Processes* (Tata McGraw-Hill Education, 2002).
[30] G. J. Székely, M. L. Rizzo, and N. K. Bakirov, Ann. Stat. **35**, 2769 (2007).
[31] S. Liu, *Distance Correlation*, MATLAB Central File Exchange (2020), retrieved September 20, 2020.
[32] J. A. Newman and K. J. Webb, Opt. Lett. **37**, 1136 (2012).
[33] J. A. Newman and K. J. Webb, Phys. Rev. Lett. **113**, 263903 (2014).
[34] W. Choi, A. P. Mosk, Q.-H. Park, and W. Choi, Phys. Rev. B **83**, 134207 (2011).
[35] S. Rotter and S. Gigan, Rev. Mod. Phys. **89**, 015005 (2017).
[36] Y.-C. Hsueh and K. J. Webb, J. Opt. Soc. Am. B **34**, 2059 (2017).
[37] D. L. Donoho, IEEE Trans. Inf. Theory **52**, 1289 (2006).
[38] N. Antipa, G. Kuo, R. Heckel, B. Mildenhall, E. Bostan, R. Ng, and L. Waller, Optica **5**, 1 (2018).
[39] P. W. Shor, SIAM Review **41**, 303 (1999).
[40] R. Pappu, B. Recht, J. Taylor, and N. Gershenfeld, Science **297**, 2026 (2002).
[41] T. J. Davis, F. Eftekhari, D. E. Gómez, and A. Roberts, Phys. Rev. Lett. **123**, 013901 (2019).
[42] D. Bouchet, S. Rotter, and A. P. Mosk, Nat. Phys. **17**, 564 (2021).
[43] A. G. Vesga, M. Hofer, N. K. Balla, H. B. D. Aguiar, M. Guillon, and S. Brasselet, Opt. Express **27**, 28384 (2019).
[44] L. Zhu, J. B. de Monvel, P. Berto, S. Brasselet, S. Gigan, and M. Guillon, Optica **7**, 338 (2020).
[45] Y. Zhou, J. Yang, J. D. Hassett, S. M. H. Rafsanjani, M. Mirhosseini, A. N. Vamivakas, A. N. Jordan, Z. Shi, and R. W. Boyd, Optica **6**, 534 (2019).
[46] COMSOL AB, Stockholm, Sweden, "Comsol multiphysics® v. 5.5," (2019).
[47] M.-C. Yang and K. J. Webb, Opt. Lett. **30**, 2382 (2005).
[48] K. J. Webb and M.-C. Yang, Phys. Rev. E **74**, 016601

(2006).
[49] M. Büttiker, Y. Imry, R. Landauer, and S. Pinhas, Phys. Rev. B **31**, 6207 (1985).
[50] P. W. Anderson, D. J. Thouless, E. Abrahams, and D. S. Fisher, Phys. Rev. B **22**, 3519 (1980).
[51] P. W. Anderson, Phys. Rev. B **23**, 4828 (1981).
[52] P. A. Mello, Phys. Rev. Lett. **60**, 1089 (1988).
[53] J.-L. Pichard and G. Sarma, J. Phys. C: Solid State Phys. **14**, L127 (1981).
[54] P. A. Mello, E. Akkermans, and B. Shapiro, Phys. Rev. Lett. **61**, 459 (1988).
[55] B. Noble and J. W. Daniel, *Applied Linear Algebra* (Prentice-Hall, 1977).
[56] K. A. Muttalib, J. L. Pichard, and A. D. Stone, Phys. Rev. Lett. **59**, 2475 (1987).
[57] J.-L. Pichard, Ph.D. thesis, University of Paris at Orsay (1984), no. 2858.
[58] R. Landauer, Philos. Mag. **21**, 863 (1970).
[59] D. C. Langreth and E. Abrahams, Phys. Rev. B **24**, 2978 (1981).
[60] P. A. Lee and A. D. Stone, Phys. Rev. Lett. **55**, 1622 (1985).
[61] D. S. Fisher and P. A. Lee, Phys. Rev. B **23**, 6851 (1981).
[62] P. A. Mello and J.-L. Pichard, J. Phys. I France **1**, 493 (1991).
[63] P. A. Mello, Phys. Rev. B **35**, 1082 (1987).
[64] N. Zanon and J.-L. Pichard, J. Phys. France **49**, 907 (1988).
[65] J.-L. Pichard, M. Sanquer, K. Slevin, and P. Debray, Phys. Rev. Lett. **65**, 1812 (1990).
[66] W. B. Davenport and W. L. Root, "Random variables and probability distributions," in *An Introduction to the Theory of Random Signals and Noise* (1987) pp. 19–44.
[67] N. G. van Kampen, "Stochastic variables," in *Stochastic Processes in Physics and Chemistry*, North-Holland Personal Library (Elsevier, Amsterdam, 2007) pp. 1–29, 3rd ed.
[68] I. A. Stegun and M. Abramowitz, *Handbook of Mathematical Functions: with Formulas, Graphs, and Mathematical Tables* (Dover Publications, 1972) this ninth Dover printing conforms to the tenth (December 1972) printing by the Government Printing Office, except for additional corrections on pages 18, 79, 80, 82, 408, 450, 786, 825, and 934.